



AN ABSTRACT OF THE DISSERTATION OF

Jeremy R. Danielson for the degree of Doctor of Philosophy in Physics  
presented on February 18, 2008.

Title: Generation of Narrowband THz Pulses and THz Studies of  
Ultrafast Phenomena in Semiconductor Quantum Wells.

Abstract approved:

---

Yun-Shik Lee

This work comprises two main parts: creating and shaping narrowband, pulsed THz radiation in a table-top optical setup; and applying THz pulses to semiconductor nanostructures to study electron dynamics.

I developed a scheme to shape the THz output of a fanned-out periodically-poled lithium niobate (PPLN) crystal. The pulses are generated by optical rectification of 800-nm pump pulses. The periodicity of the PPLN determines the exact THz frequency, and the PPLN crystal was grown in such a way that different regions of the crystal generated different THz frequencies. Spatial filtering controls the power spectrum of the output pulses, which we measured by electro-optic detection in a nonlinear crystal.

I created an optical arrangement to generate tunable, narrowband THz radiation by difference-frequency generation in zinc telluride (ZnTe). A single, chirped pump pulse was used for the optical source, and the difference-frequency was obtained by mixing two chirped optical pulses with a relative time delay in a ZnTe crystal. The generated THz pulse energy was measured using a silicon bolometer, revealing conversion efficiencies as high as  $4 \times 10^{-6}$ . Using a Michelson interferometer, the THz field autocorrelation was also measured, showing tunability of the emitted field with a spectral range of 0.5 - 2.2 THz.

I used THz radiation as a tool for examining excitonic states in GaAs quantum wells. The optical transmission spectra of these quantum wells were observed near the light-hole and heavy-hole excitonic 1s resonance lines around 800 nm. The spectral modulation of the exciton resonances was measured as intense single-cycle THz radiation was applied, reaching field strengths as high as 10 kV/cm. By varying the delay between the IR probe pulse and the THz driving pulse, I observed coherent, transient extreme-nonlinear effects in the transmission spectra.

©Copyright by Jeremy R. Danielson

February 18, 2008

All Rights Reserved

Generation of Narrowband THz Pulses and THz Studies of Ultrafast  
Phenomena in Semiconductor Quantum Wells

by

Jeremy R. Danielson

A DISSERTATION

submitted to

Oregon State University

in partial fulfillment of

the requirements for the

degree of

Doctor of Philosophy

Presented February 18, 2008

Commencement June 2008

Doctor of Philosophy dissertation of Jeremy R. Danielson

presented on February 18, 2008

APPROVED:

---

Major Professor, representing Physics

---

Chair of the Department of Physics

---

Dean of the Graduate School

I understand that my dissertation will become part of the permanent collection of Oregon State University libraries. My signature below authorizes release of my dissertation to any reader upon request.

---

Jeremy R. Danielson, Author

# TABLE OF CONTENTS

	<u>Page</u>
1. Overview of THz TDS Spectroscopy.....	1
1.1 Terahertz Radiation, Sources and Detectors.....	1
1.2 Optical Rectification in Nonlinear Crystals.....	8
1.3 Characterization of THz Pulses.....	22
2. Generation of Shaped, Multiple-Cycle THz Pulses in PPLN.....	36
2.1 Narrowband THz Generation in PPLN.....	36
2.2 Shaping THz pulses emitted from FO-PPLN.....	39
3. Creating Multiple-Cycle Pulses through Difference-Frequency Generation.....	44
3.1 Difference Frequency Generation Using Chirped Pulses.....	44
3.2 Experimental Arrangement.....	52
3.3 Measurements.....	53
4. THz-Driven, Nonlinear Transient Effects in Semiconductor Quantum Wells.....	59
4.1 Excitonic Structure in Semiconductor Quantum Wells.....	60
4.2 Experimental Investigation.....	65
5. Conclusion.....	75
Bibliography.....	77
Appendix: Bolometer Sensitivity for a Pulsed THz Source.....	82

# LIST OF FIGURES

<u>Figure</u>	<u>Page</u>
1.1 Rectified Polarization vs. Time.....	11
1.2 Emitted Field vs. Time.....	12
1.3 Spectrum of Emitted Field.....	12
1.4 ZnTe Absorption Curve.....	15
1.5 Driving Field in the Crystal Frame.....	17
1.6 THz Power as a Function of Crystal Angle.....	18
1.7 Polarization Angles of the Fields.....	19
1.8 THz Polarization in Lab Frame.....	20
1.9 ZnTe Emission Curves.....	21
1.10 Field Autocorrelation Arrangement.....	22
1.11 Typical Field Autocorrelation.....	24
1.12 Intensity Autocorrelation Arrangement.....	25
1.13 THz Polarization in an Electro-Optic Crystal.....	29
1.14 Electro-Optic Sampling Arrangement.....	32
2.1 Periodically-Poled Lithium Niobate.....	37
2.2 Fanned Out PPLN.....	38
2.3 THz Frequency vs. Domain Length.....	39
2.4 Pulse Shaping Arrangement.....	40
2.5 Spectral Filtering of FO-PPLN Output.....	42

## LIST OF FIGURES (Continued)

<u>Figure</u>	<u>Page</u>
3.1 The Chirped Pulse.....	46
3.2 Group Velocity Dispersion Arrangements.....	47
3.3 Pulse Delay Arrangement.....	48
3.4 THz Power vs. Angle.....	51
3.5 Example THz Field Autocorrelation.....	53
3.6 THz Spectrum vs Pulse Delay.....	53
3.7 Power vs THz frequency for Various Pulse Durations.....	55
3.8 THz Power Asymmetry for Negative Delay.....	56
3.9 THz Power vs. Pump Power.....	58
4.1 Quantum Well Potential.....	60
4.2 Band Structure for Carriers Traveling in the QW Plane.....	61
4.3 Experimental Arrangement for THz-Driven Spectral Modulation..	65
4.4 $1-T(\omega)$ for the QW sample.....	66
4.5 Differential Transmission Spectra.....	71
4.6 Differential Transmission vs. Time.....	71
A.1 CW THz Signal.....	83
A.2 Pulsed THz Signal.....	83

# Generation of Narrowband THz Pulses and THz Studies of Ultrafast Phenomena in Semiconductor Quantum Wells

## 1. Overview of THz TDS Spectroscopy

### 1.1 Terahertz Radiation, Sources and Detectors

The terahertz (THz) section of the electromagnetic spectrum refers loosely to electromagnetic radiation with frequency  $0.1 \times 10^{12}$  to  $10 \times 10^{12}$  Hz. The corresponding wavelength range is 30  $\mu\text{m}$  to 3 mm, and the energy range is 0.4 to 40 meV. It is commonly referred to as far-infrared radiation or submillimeter radiation due to its wavelength.

In the laboratory of Dr. Yun-Shik Lee at Oregon State University, I have conducted a number of studies into methods for generating and shaping specific THz pulses, as well as applying these pulses to the study of carrier dynamics in semiconductor nanostructures.

In the first chapter I introduce the methods we employ for generation of THz radiation, specifically optical rectification. I also discuss some of the methods we've used to characterize THz pulses such as electro-optic sampling and field autocorrelation.

In the second chapter I discuss work I've done in shaping THz pulses generated in a fanned-out, periodically-poled lithium niobate crystal. We take advantage of the crystal structure to generate a range of selectable THz frequencies. This chapter is based on our published work in Applied Physics Letters [1].

The third chapter discusses a novel arrangement we've developed for the generation of narrowband THz radiation. This arrangement has the advantage of being pulsed and easily tunable, and uses a single mode-locked femtosecond laser as its pumping source. This work is being submitted for publication in the Journal of Applied Physics.

In the fourth chapter, I describe a study in which the excitonic states of a GaAs quantum well are driven by THz frequency pulses, and probed with optical frequency light. This work has observed coherent and transient excitonic effects which are nonlinear in the THz driving field. The experiment was conducted in concert with a theoretical investigation by M. Hanno and S.W. Koch at Phillips University in Marburg, Germany. This work was presented to CLEO in May 2007 and was published in Physical Review Letters in December 2007 [2].

### **1.1.1 Terahertz Studies**

Terahertz radiation is as useful as any other region of the electromagnetic spectrum. Just as there are a myriad of uses for visible light, infrared radiation, or radio-frequency regions of the spectrum, the far-infrared portion of the spectrum is uniquely situated for a number of purposes.

The photon energy of THz radiation is too low for atomic transitions, and does not directly excite electrons in semiconductors. Because of this, it will penetrate many materials that will absorb visible light, such as plastics and silicon wafers. Unlike

microwaves, THz radiation has a sufficiently small wavelength that it can discern small structures of submillimeter size [3,4,5]. It can therefore be used for a number of imaging applications, such as scanning for material defects, scanning for weapons and explosives [6], and in the area of medical imaging. There are a number of molecular and vibrational modes in the THz regime, so THz radiation can be used to differentiate between different tissue “signatures”. Unlike X-rays, THz radiation is non-ionizing, and is therefore not expected to damage living cells and tissue. For this reason, there has been a lot of interest in “T-rays” in the area of medical imaging of skin, teeth, and other tissues [7].

Because there are so many molecular resonances in the THz region, there are many spectroscopic applications. THz has been used to study rotational and torsion dynamics of molecules [8,9] and protein folding dynamics [10]. It can also be used for molecular identification. Possible applications include identification of chemical and biological agents [11], pharmaceutical differentiation between drug polymorphs [8], remote sensing for atmospheric and pollution studies [12], and solar system studies [13, 14]. For spectroscopic analysis, THz radiation has an advantage over optical spectroscopy in that its oscillations are slow enough for time-domain recording of the electric field. This yields not only frequency information of the THz response, but phase information as well, opening the door to real dynamic spectroscopic studies.

THz has proven quite useful in studies of carrier dynamics in semiconductors. The photon energy of 1-10 meV corresponds with a number of electronic effects such as excitons, plasmons, impurity localization, and magnetic level-splitting. It also

corresponds to electronic resonances in semiconductor nanostructures such as quantum wells and quantum dots. Since carrier and coherence relaxation times are typically on the order of picoseconds, THz frequencies are sufficiently fast for dynamic studies of carrier effects. These studies are important for development of devices such as optical modulators and quantum well qubit systems, as well as miniaturization of semiconductor devices.

THz frequencies are also quite useful for material characterization. It couples easily to phonon modes and can be used to study lattice dynamics. Additionally, it is slow enough to cause large carrier motions, and can be used for conductivity studies and characterization. This has an advantage in characterizing bulk carrier and crystal properties without contacting or destroying a sample, being a “contact-less” method.

### **1.1.2 Terahertz Sources**

Terahertz studies have been somewhat limited in the past, due to a lack of convenient sources. THz photon energies are too low for atomic transitions, ruling out atomic sources; and electronic sources are limited to gigahertz frequencies. Even so, a number of THz sources have been developed:

**Black-body** sources take advantage of the wide range of energies emitted from a warm emitter. One can use filtering to extract the desired frequency range. The

radiation gained in this way is continuous and incoherent, but can be useful for absorption studies.

**Free electron lasers (FEL)** take advantage of the synchrotron radiation emitted by accelerating electrons and passing them through an array of transverse magnetic fields, alternating in their polarity. The resulting acceleration of the electron beam produces coherent radiation which is widely tunable by altering the magnetic field array. While FELs give strong, coherent THz radiation, they require a great deal of space and are expensive, being limited to a number of user-facilities.

**Backward Wave Oscillators** follow a similar principle to FELs. Electrons are emitted from an electron gun and passed through an array of electrodes which slow them. A coherent GHz – THz beam is formed in the direction opposite the electron beam's. The emitted frequency is determined by both the electrode spacing and the accelerating voltage in the electron gun, both of which are adjusted to tune the emission

**Molecular gas lasers**, using gasses like CO<sub>2</sub>, have been created which emit in the THz spectrum. These lasers take advantage of the lower energies of molecular state transitions to emit in the MeV regime. These lasers give coherent THz

radiation with highly precise lines, but suffer from low output powers and a lack of tunability.

**Frequency Mixing** has also been used to create THz radiation. Two optical beams of slightly different frequency are sent into a resonance cavity, enhancing their interior field strengths. They are then passed through a crystal with a large second-order susceptibility such as GaAs. The two frequencies mix in the crystal, resulting in THz emission through difference-frequency generation.

The sources listed above share the property of being continuous-wave sources. Since the advent of the femtosecond mode-locked laser, pulsed sources have been developed, taking advantage of the short duration of the mode-locked pulse.

**Photoconductive antenna arrays** are made from semiconductors placed between two electrodes at different voltages. Photo-excitation by an incident beam injects carriers into the material, which are accelerated by the electrodes, causing the emission of EM radiation. Assuming a sufficiently short carrier lifetime the current in the antenna will be proportional to the envelope of the exciting pulse. Given a pulse of duration  $\sim 1$ ps, the emitted radiation will be in the THz spectrum. For a PC antenna, the emitted frequencies are limited by the carrier relaxation rate, and frequencies as high as 3 THz have been obtained.

**Optical Rectification** in nonlinear crystals also generates THz radiation using the short pulse duration of a femtosecond pulse. In this arrangement, a pulse is sent into a nonlinear crystal with a strong second-order susceptibility, resulting in a rectification of the polarization. This rectified polarization lasts as long as the pulse, and is proportional to the envelope of the pumping pulse. Similar to the PC antenna, it emits a frequency spectrum given by the duration of the driving pulse.

These two sources have the property of being pulsed, allowing them to be used to probe dynamic processes in materials. Additionally, they can be installed easily into an optics lab containing a femtosecond laser. Finally, while the average power of these sources is not very high (on the order of nanowatts) the energy of the pulses is compressed within very short time scales, giving peak powers of 5 kW and peak electric fields of 10 keV.

### **1.1.3 Terahertz Detectors**

There are a limited number of ways of detecting THz radiation. The photon energy is well below the bandgap of most semiconductors, so phototransistors will not work. Calorimeters are commonly employed as detectors, measuring the energy deposited from the THz source. Examples of these are bolometers and Golay cells. THz bolometers measure the change in photoresistivity of a chilled silicon sample

when heated by the THz beam. A Golay cell measures the expansion of gas in a cell due to temperature changes.

For short-pulse THz radiation, PC antennae and nonlinear crystals can be employed. Both use an optical probe pulse to sample the incident THz field. In the PC detector, the short optical probe creates photocarriers, which are accelerated by the THz electric field, acting as a bias. The resulting photocurrent is then measured and the THz field is mapped out as a function of the delay between the optical and THz pulse. Nonlinear crystal detectors take advantage of the electro-optic effect, in which the THz field induces a temporary birefringence in the crystal. The polarization of a short optical pulse is rotated by this birefringence, which is then detected and correlated to the THz field in the same way. I will discuss this technique further when describing our methods.

## **1.2 Optical Rectification in Nonlinear Crystals**

One common method of creating THz frequency pulses is through the optical rectification of ultrashort laser pulses. In this technique one takes advantage of the nonlinear response of various optical materials to create a low-frequency pulse from a driving optical frequency pulse.

### 1.2.1 Nonlinear Optical Responses

The linear response of a material's polarization to a driving EM field is given by  $\vec{P} = \chi \vec{E}$ , where  $\chi$  is the susceptibility tensor. For isotropic materials,  $\chi$  can be reduced to a constant. To model nonlinearities in the material's optical response, this relation is generalized in the form of a Taylor series

$$P_i = \chi^{(1)}_{ij} E_j + \chi^{(2)}_{ijk} E_j E_k + \chi^{(3)}_{ijkl} E_j E_k E_l + \dots \quad (1.2.1)$$

where summation over repeated indices is implied. The number in parentheses over each tensor is the order of the susceptibility component. Optically responsive materials commonly have first and third order responses. Nonzero second order susceptibilities are less common, as the primary condition for them is a lack of inversion symmetry. This requires an ordered crystal structure in which an asymmetric bonding pattern exists. Examples of such crystals are GaAs, ZnTe, GaSe, and LiNbO<sub>3</sub>.

### 1.2.2 Frequency Dependence of the Response

Consider a single-frequency beam incident on an optical crystal. Its electric field can be described as  $\vec{E}(t) = E_0 \cos(\omega t) = \frac{\vec{E}_0}{2} [\exp(-i\omega t) + \exp(i\omega t)]$ . Retaining the first two terms in the polarization expansion,

$$\begin{aligned}
P_i = & \frac{1}{2} \chi^{(1)}_{ij} E_{0j} \exp(-i\omega t) + c.c. \\
& + \frac{1}{2} \chi^{(2)}_{ijk} E_{0j} E_{0k} [\exp(-2i\omega t) + \exp(0) + c.c.]
\end{aligned}
\tag{1.2.2}$$

The first term describes the linear response of the material and leads to linear optic effects such as attenuation and a change in phase velocity. It is important to note that while the polarization may have a phase shift relative to the incoming wave, it oscillates at the same frequency. As a result, there will be no frequency conversion as a result of the linear susceptibility.

The second term, on the other hand, contains a term of frequency  $2\omega$  and as well as a non-oscillating term. The first leads to frequency doubling, and the second leads to a nonzero offset, or rectification, in the polarization.

### 1.2.3 Rectification of an Ultrashort Pulse

Now consider an incident pulse which has central frequency  $\omega$  and a gaussian envelope parameterized by  $\tau$ :

$$E_{opt}(t) = E_0 \cos(\omega t) \exp\left(-\frac{t^2}{\tau^2}\right)
\tag{1.2.3}$$

Assume the envelope is varying slowly with respect to the carrier wave, so that the electric field can be considered monochromatic. I suppress the vector nature of the polarization, which will be discussed in detail later. In this approximation, the rectified polarization has time dependence

$$P_R(t) \propto \left( \exp\left(-\frac{t^2}{\tau^2}\right) \right)^2 = \exp\left(-\frac{t^2}{\left(\frac{\tau}{\sqrt{2}}\right)^2}\right) \quad (1.2.4)$$

as represented in fig. 1.1.

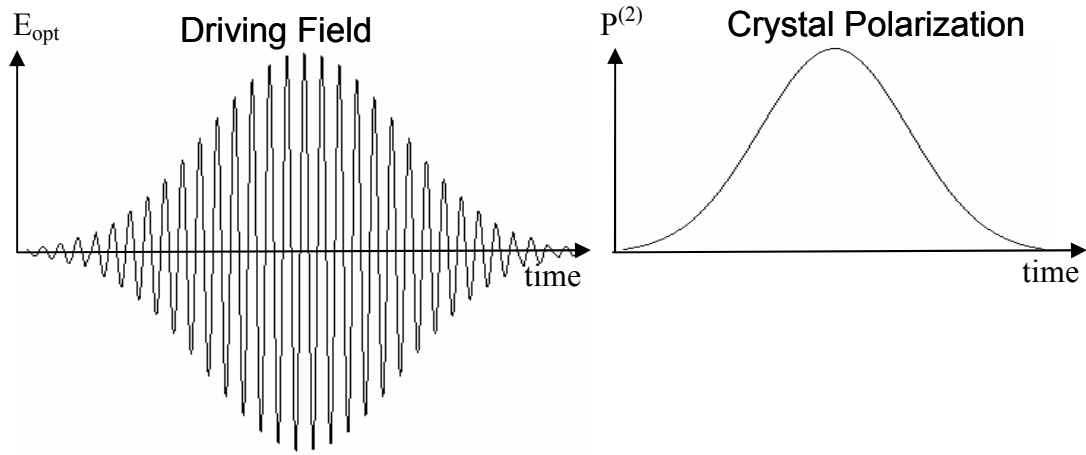


Fig 1.1: Rectified Polarization vs. Time. The rectified polarization follows the envelope of the driving pulse, and does not oscillate.

The time dependence of the emitted field is given by

$$E_R(t) \propto \frac{d^2}{dt^2} P_R(t) \quad (1.2.5)$$

$$= \frac{d^2}{dt^2} \exp\left(-\frac{t^2}{\left(\frac{\tau}{\sqrt{2}}\right)^2}\right) \quad (1.2.6)$$

$$= \frac{8}{\tau^4} \exp\left(-\frac{t^2}{\left(\frac{\tau}{\sqrt{2}}\right)^2}\right) \cdot \left(2t^2 - \frac{\tau^2}{2}\right)$$

shown in fig 1.2.

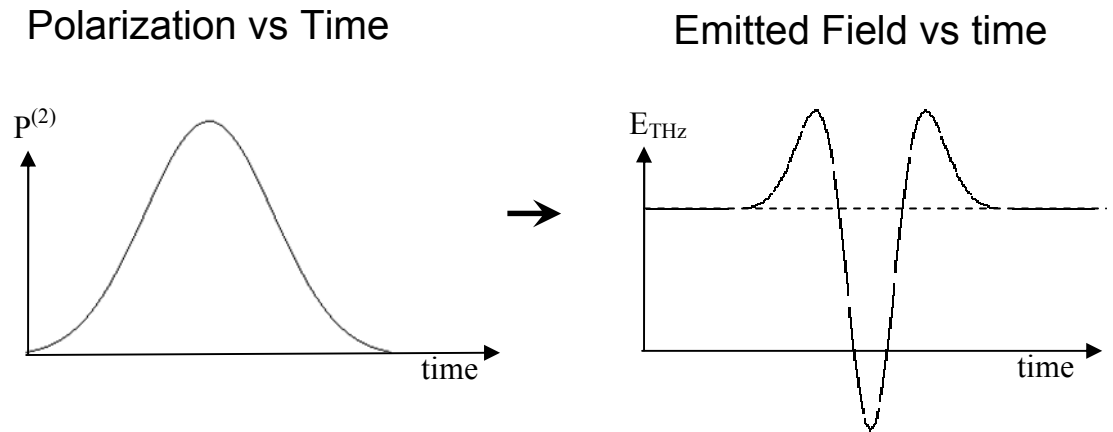


Fig 1.2: Emitted Field vs. Time. The emitted field follows the curvature of the rectified polarization.

The spectrum of the emitted pulse is given by

$$\tilde{E}_R(\omega) = \left( \sqrt{\frac{\pi}{2}} \tau \right) \omega^2 \exp\left( -\frac{1}{8} \omega^2 \tau^2 \right) \quad (1.2.7)$$

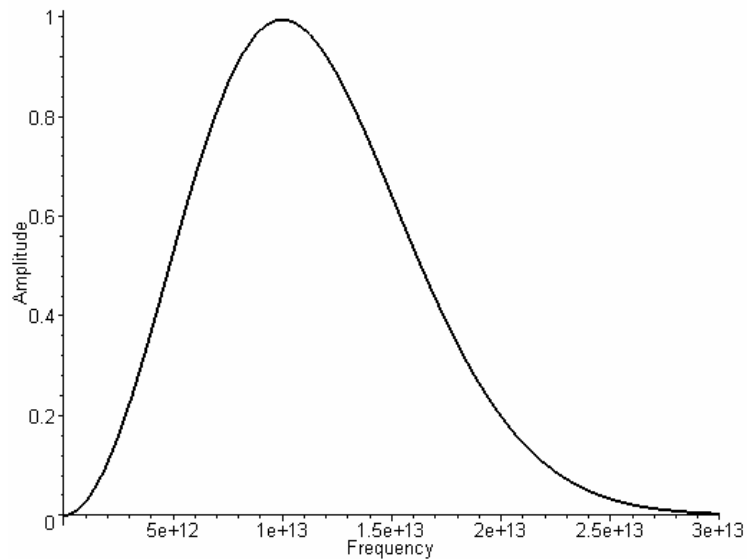


Fig 1.3: Spectrum of Emitted Field. Emission spectrum for a rectified 90 fs pulse, not accounting for propagation effects.

As shown Fig 3, by rectifying a sufficiently short pulse (typically 90 fs in the lab), one can create THz frequency pulses.

#### **1.2.4 Effects of Propagation through a nonlinear crystal**

For an infinitely thin nonlinear crystal, the description above would suffice to calculate the shape of the emitted THz pulse. Unfortunately, the signal would also be vanishingly weak. In the calculations above, the expected THz signals are much higher frequency (~20 THz) than those typically created in the lab with this method. To create a real THz pulse, the pump beam must be sent through a finite slab of material, and propagation effects in nonlinear crystals play an important role.

#### **1.2.5 Dispersion and Walk off Length**

If the THz and optical pulse have the same velocity traveling through the nonlinear crystal, the THz field will continue to build up through the entire crystal. In reality, the THz and optical pulses will have a velocity mismatch. As they propagate, the THz pulse will fall behind or get ahead of the optical pulse. After traveling a certain distance through the crystal, the THz created by the optical pulse will be 180° out of phase with the THz waves created previously, and they will destructively interfere. This distance is called as the walk-off length.

Since the group velocities of the two pulses are determined by the material and frequencies used, it is impossible to perfectly match the phase velocity of every

frequency component of the THz pulse. This puts a limit on how thick a nonlinear crystal should be to maximize its emission. For ZnTe, the walk-off length between an 800 nm pulse and 0.5-2.5 THz pulse is on the order of 1-2 mm [15]. For THz frequencies outside this range, the velocity matching is worse, and those frequencies will be filtered out.

All nonlinear crystals exhibit some dispersion. For ZnTe, the index of refraction drops from 3.4 at 0.5 THz to 3.2 at 2 THz. Aside from affecting the walk-off lengths mentioned above, this will also cause the THz pulse to broaden in time and reduce its peak power as its frequency components become spread out.

### **1.2.6 THz Absorption**

THz photons tend to match phonon energies in most materials, so absorption plays a significant role in propagation through a nonlinear crystal. Most crystals used for optical rectification have a transverse-optical phonon resonance between 5-10 THz. ZnTe, for example, has a TO phonon resonance at 5 THz (shown in fig. 1.4). Not only does this act as a low-pass filter below 5 THz, but there are also many other influences on the absorption spectra such as two-photon processes. As a result, there is significant frequency filtering in ZnTe above 3 THz.

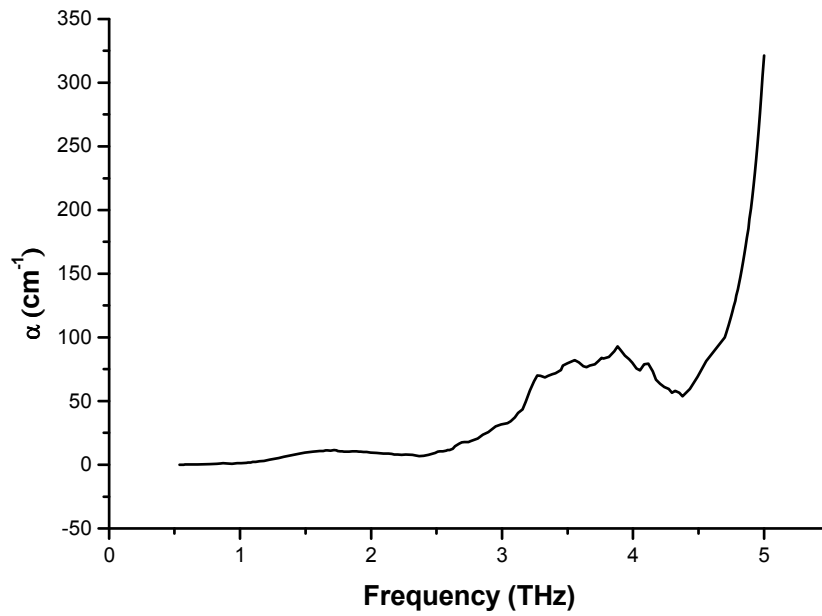


Fig. 1.4: ZnTe Absorption Curve [16].

### 1.2.7 Polarization Considerations

In the following discussion, I will be dealing mainly with second order susceptibilities. Assuming the indices are permutable, one can redefine the nonlinear susceptibility with the so-called d-matrix [17]

$$d_{il} = \frac{1}{2} \chi_{ijk}^{(2)} \quad (1.2.8)$$

Making the identifications

$$\begin{array}{l} l \quad 1 \quad 2 \quad 3 \quad 4 \quad 5 \quad 6 \\ jk \quad 11 \quad 22 \quad 33 \quad 23,32 \quad 13,31 \quad 12,21 \end{array}$$

this allows one to write the second order d-matrix:

$$\begin{pmatrix} P_x \\ P_y \\ P_z \end{pmatrix} = 2\varepsilon_0 \begin{pmatrix} d_{11} & d_{12} & d_{13} & d_{14} & d_{15} & d_{16} \\ d_{21} & d_{22} & d_{23} & d_{24} & d_{25} & d_{26} \\ d_{31} & d_{32} & d_{33} & d_{34} & d_{35} & d_{36} \end{pmatrix} \cdot \begin{pmatrix} E_x^2 \\ E_y^2 \\ E_z^2 \\ 2E_y E_z \\ 2E_z E_x \\ 2E_x E_y \end{pmatrix} \quad (1.2.9)$$

This allows one to write the crystal susceptibilities as a two dimensional array. Crystal symmetries generally reduce this matrix further, forcing a number of components to zero and reducing the number of degrees of freedom. For example, ZnTe and GaAs both share the zincblende structure, for which the d-matrix is

$$\begin{pmatrix} 0 & 0 & 0 & d_{14} & 0 & 0 \\ 0 & 0 & 0 & 0 & d_{14} & 0 \\ 0 & 0 & 0 & 0 & 0 & d_{14} \end{pmatrix} \quad (1.2.10)$$

The linear susceptibility of ZnTe is isotropic, so changing the orientation of the incident field will not change the phase-matching of the optical and THz pulses. However, because of the tensor nature of the second-order susceptibility, it will affect the efficiency of the rectification process. Consider a ZnTe crystal cut so that its surface is normal to the [110] crystal axis. This is typical to maximize THz emission. The polarization of the incident optical field will lie somewhere in the [001]×[-110] plane, as shown in fig. 1.5. Let the angle between the optical field and [001] axis be  $\theta$ .

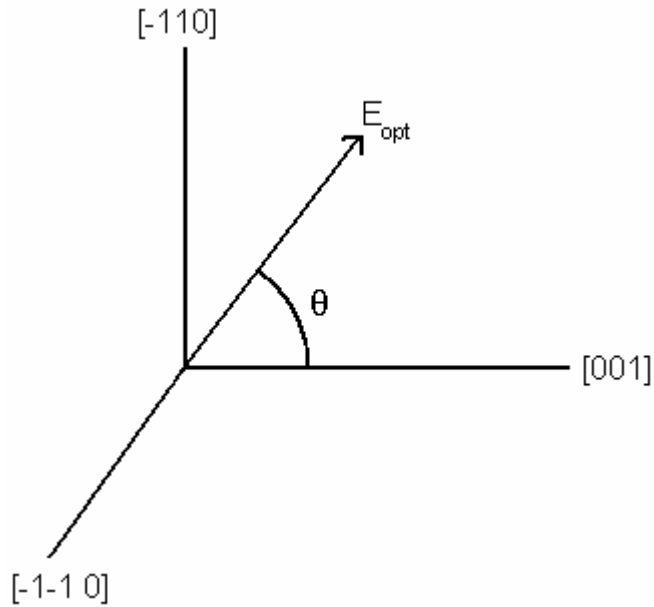


Fig 1.5: Driving Field in the Crystal Frame

The optical field can be described as

$$E_{opt} = \left[ \hat{z} \cos \theta + \frac{1}{\sqrt{2}}(-\hat{x} + \hat{y}) \sin \theta \right] \cdot E(t) \quad (1.2.11)$$

where  $E(t)$  is the time-dependence of the field. Inserting this into the second-order polarization equation,

$$\begin{pmatrix} P_x^{(2)} \\ P_y^{(2)} \\ P_z^{(2)} \end{pmatrix} = 2\varepsilon_0 d_{14} \begin{pmatrix} 0 & 0 & 0 & 1 & 0 & 0 \\ 0 & 0 & 0 & 0 & 1 & 0 \\ 0 & 0 & 0 & 0 & 0 & 1 \end{pmatrix} \cdot \begin{pmatrix} \frac{1}{2} \sin^2 \theta \\ \frac{1}{2} \sin^2 \theta \\ \cos^2 \theta \\ \sqrt{2} \sin \theta \cos \theta \\ -\sqrt{2} \sin \theta \cos \theta \\ -\sin^2 \theta \end{pmatrix} \cdot E(t)^2 \quad (1.2.12)$$

Neglecting the factors independent in angle,

$$\vec{P}^{(2)} \propto \hat{z}(-\sin^2 \theta) + \frac{1}{\sqrt{2}}(-\hat{x} + \hat{y}) \cdot (-2 \sin \theta \cos \theta) \quad (1.2.13)$$

Squaring this gives the emitted THz power as a function of angle

$$|\vec{P}^{(2)}|^2 = \sin^4 \theta + 4 \sin^2 \theta \cos^2 \theta \quad (1.2.14)$$

giving a strong angular dependence to the power, shown in fig 1.6. The THz emission goes to zero when the driving optical field is aligned with the [001] axis. In practice, we see some divergence from this calculation due to third-order effects such as carrier excitation.

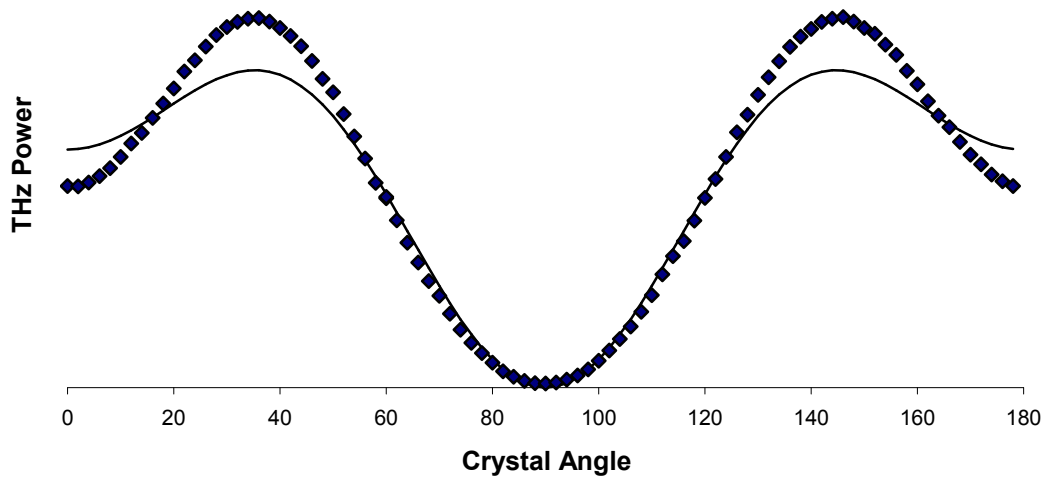


Fig 1.6: THz Power as a Function of Crystal Angle. The dots are measured powers for various crystal rotations, where the angle is measured from the [110] axis. The solid line is the calculated amount. While the angular dependence agrees with the second-order calculation, there is some difference in the measured values.

The emitted THz polarization is an important parameter, especially when detected through electro-optic sampling. The direction of the THz polarization above is given by

$$\tan \phi \tan \theta = 2 \quad (1.2.15)$$

where  $\phi$  is the THz polarization relative to the  $[001]$  axis of the crystal. This is shown in fig. 1.8. In the lab, the driving polarization is typically held constant and the crystal itself rotated. For a rotation  $\theta_L$  in the lab frame, the pump polarization undergoes an opposite rotation  $\theta = -\theta_L$  in the crystal frame. Therefore the THz polarization in the lab frame should actually be given by  $\phi_L = \phi + \theta_L$ , as seen in fig. 1.7.

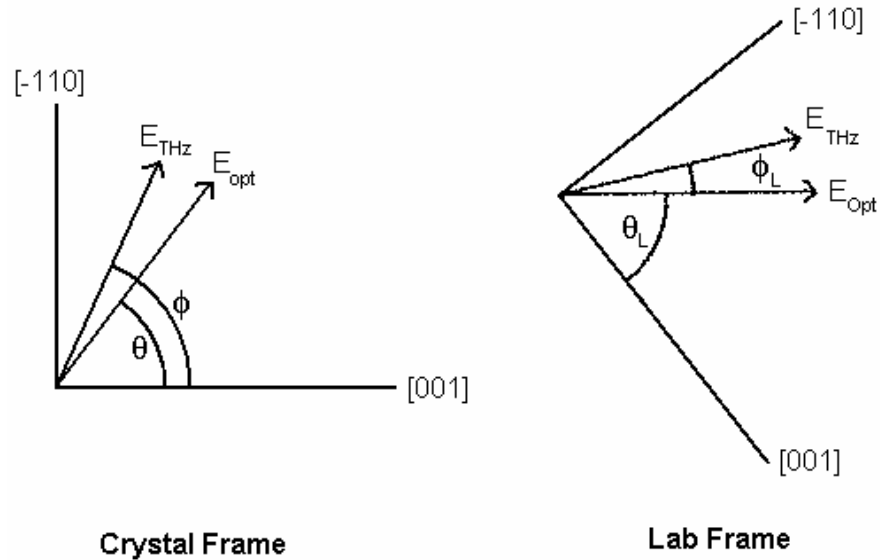


Fig 1.7: Polarization Angles of the Fields.

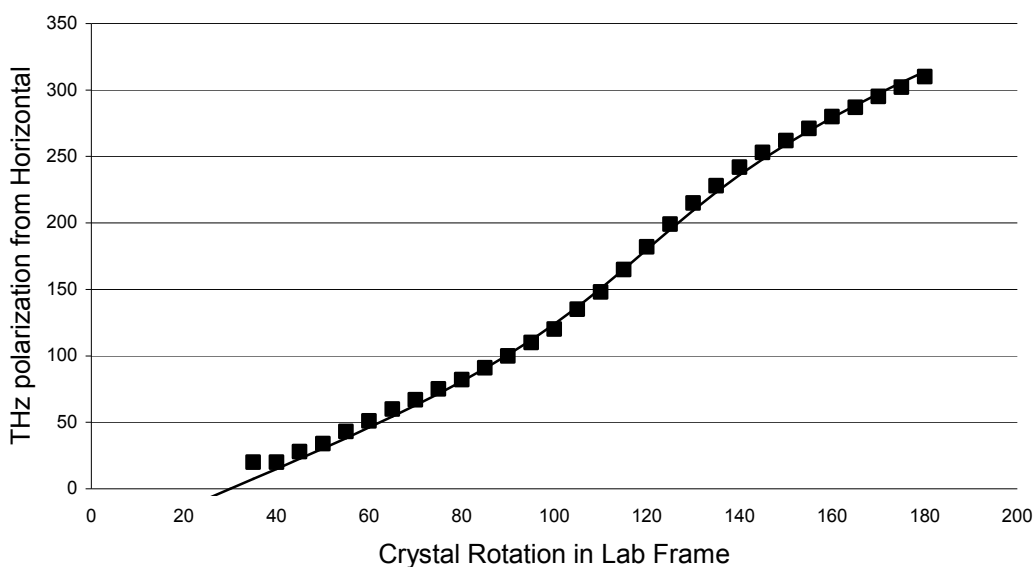


Fig 1.8: THz Polarization in the Lab Frame. The dots represent polarization measurements made using a wire grating. The line is the calculated polarization. All angles are measured from horizontal.

### 1.2.8 Conversion Efficiency

Using optical rectification in ZnTe, we typically create pulses with a spectrum of 0.5 – 2 THz and pulse energy of ~100 nJ. Being a second-order process, the emitted THz field strength is proportional to the square of the driving field strength. Similarly, the THz power should be quadratic with the driving pump power. In practice, this is true for lower optical pulse energies but becomes inaccurate for fluence greater than  $5 \times 10^8 \text{ W/cm}^2$ , corresponding to 350 mJ pulses in a typical configuration. Fig. 1.9 shows that above this value, the conversion efficiency (THz pulse energy / Optical pulse energy) becomes constant with increasing power, indicating the process is no

longer quadratic. This is typical in ZnTe, and can be attributed to various parasitic processes such as free carrier generation. [18]

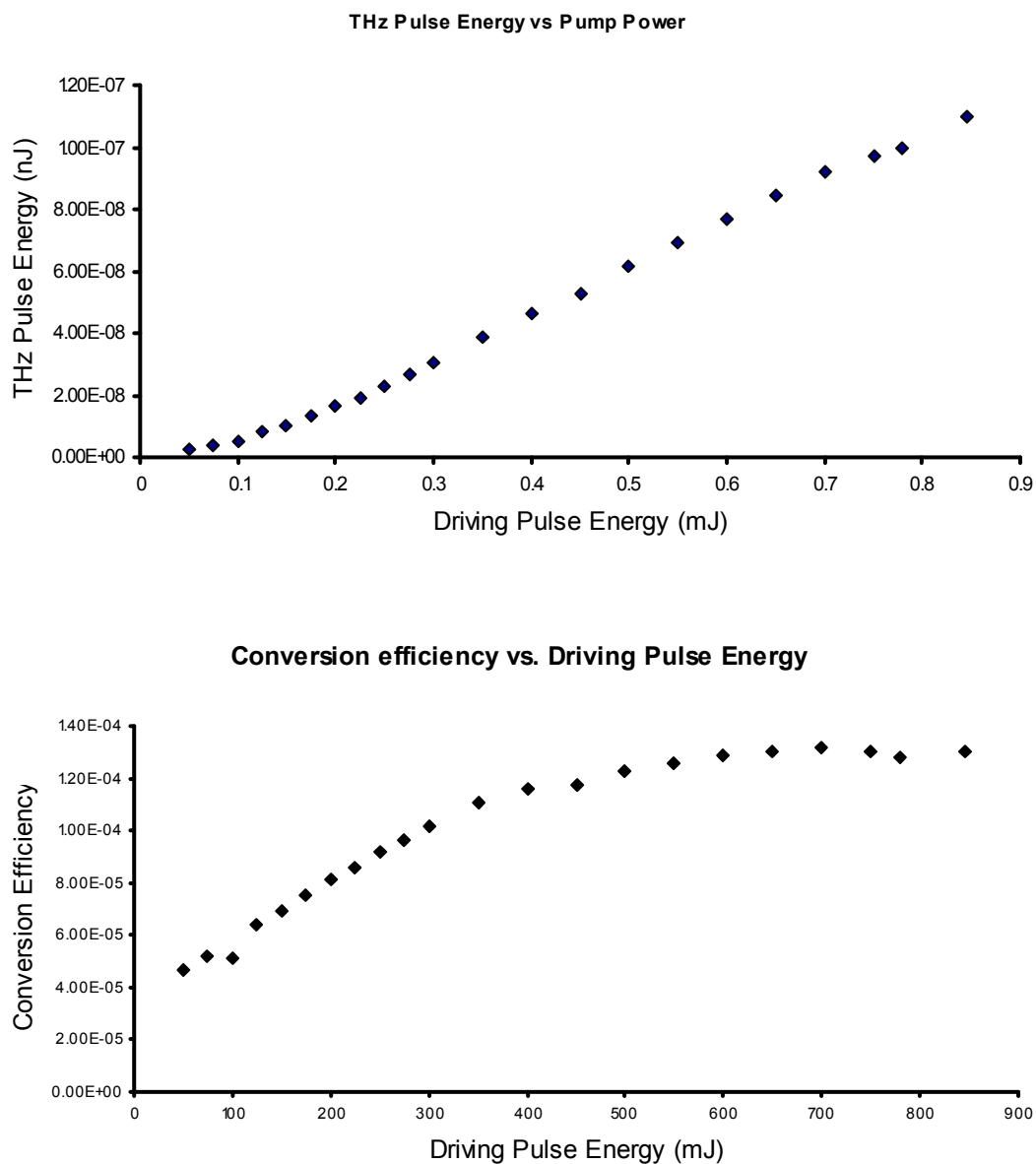


Fig. 1.9: ZnTe Emission Curves. THz pulse energy emitted from a ZnTe crystal was measured when driven by a 90 fs, 800 nm pulse. The top graph shows the emitted THz power as the driving pulse is increased in energy. The second graph shows the conversion efficiency,  $E_{\text{THz}}/E_{\text{opt}}$ .

### 1.3 Characterization of THz Pulses

While calorimeters can measure the energy of THz pulses, they do not provide information about their frequency or dynamic qualities. To measure these, we have employed the techniques of interferometry and electro-optic sampling.

#### 1.3.1 Autocorrelations

An interferometric autocorrelation can be used to determine the frequency spectrum of a THz pulse. The detection arrangement is quite simple (fig 1.10), consisting of a Michelson interferometer whose output is sent to a power detector such as a bolometer. Fig. 1.11 shows a representative autocorrelation signal.

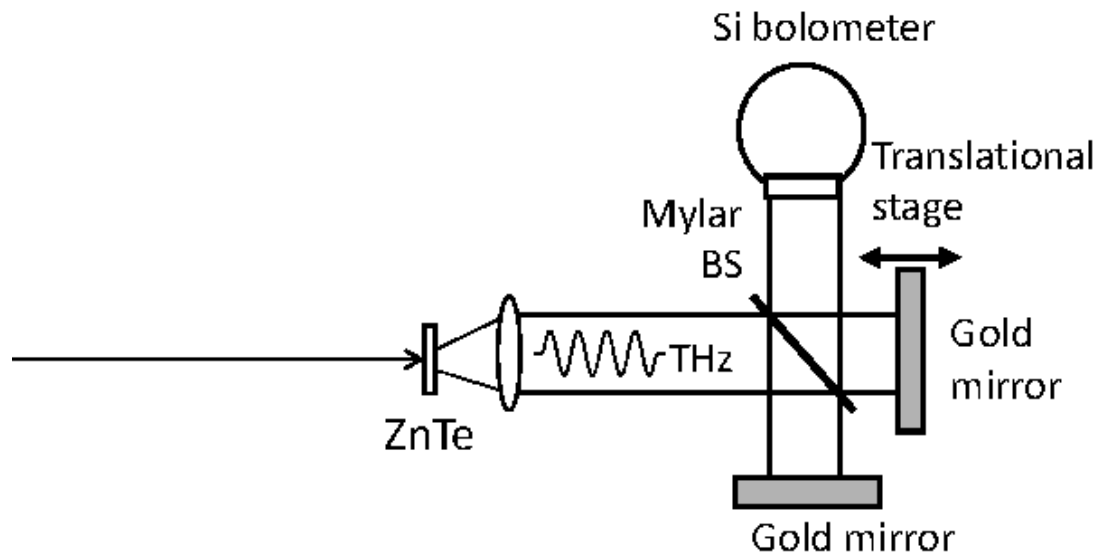


Fig 1.10: Field Autocorrelation Arrangement.

The power as a function of path delay is measured and follows the form

$$I(\tau) = \int_{-\infty}^{\infty} dt |E(t) + E(T - \tau)|^2 \quad (1.3.1)$$

which expands to

$$I(\tau) = \int_{-\infty}^{\infty} dt [E(t)^2 + E(T - \tau)^2] + 2 \int_{-\infty}^{\infty} dt E(t)E(T - \tau) \quad (1.3.2)$$

The first integral is constant with delay  $\tau$ , and can be neglected for the purpose of characterizing the pulse. The second integral varies with delay, and is proportional to the field autocorrelation

$$A(\tau) = \int_{-\infty}^{\infty} dt E(t)E(T - \tau) \quad (1.3.3)$$

Applying a fourier transform on the autocorrelation,

$$\tilde{A}(\omega) = \int_{-\infty}^{\infty} A(\tau)e^{i\omega\tau} d\tau \quad (1.3.4)$$

$$\begin{aligned} &= \int_{-\infty}^{\infty} d\tau \int_{-\infty}^{\infty} dt e^{i\omega\tau} E(t)E(T - \tau) \\ &= \frac{1}{(2\pi)^2} \int_{-\infty}^{\infty} d\tau e^{i\omega\tau} \int_{-\infty}^{\infty} dt \int_{-\infty}^{\infty} d\omega_1 \tilde{E}(\omega_1) e^{-i\omega_1 t} \int_{-\infty}^{\infty} d\omega_2 \tilde{E}(\omega_2) e^{-i\omega_2 t} \\ &= \frac{1}{(2\pi)^2} \int_{-\infty}^{\infty} d\tau \int_{-\infty}^{\infty} d\omega_1 \int_{-\infty}^{\infty} -d\omega_2 (2\pi) \delta(\omega_1 - \omega_2) e^{i\omega\tau} e^{i\omega_2 t} \tilde{E}(\omega_1) \tilde{E}(-\omega_2) \\ &= \frac{1}{2\pi} \int_{-\infty}^{\infty} d\tau \int_{-\infty}^{\infty} d\omega_2 e^{-i\omega_2 t} e^{i\omega\tau} \tilde{E}(\omega_2) \tilde{E}(-\omega_2) \\ &= \frac{1}{2\pi} \int_{-\infty}^{\infty} d\omega_2 (2\pi) \delta(\omega - \omega_2) |\tilde{E}(\omega_2)|^2 \\ &= |\tilde{E}(\omega)|^2 \end{aligned}$$

The Fourier transform of the field autocorrelation is the power spectrum of the THz pulse.

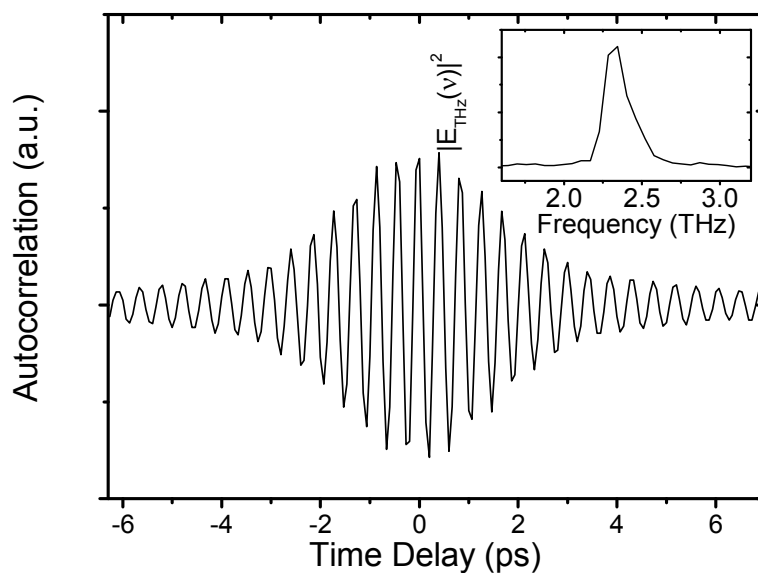


Fig 1.11: Typical Field Autocorrelation

This characterization technique is similar to an intensity autocorrelator, which is used to characterize ultrashort optical pulses. Because it is in common use and optical pulse durations are central to THz pump-probe spectroscopy, I describe it here.

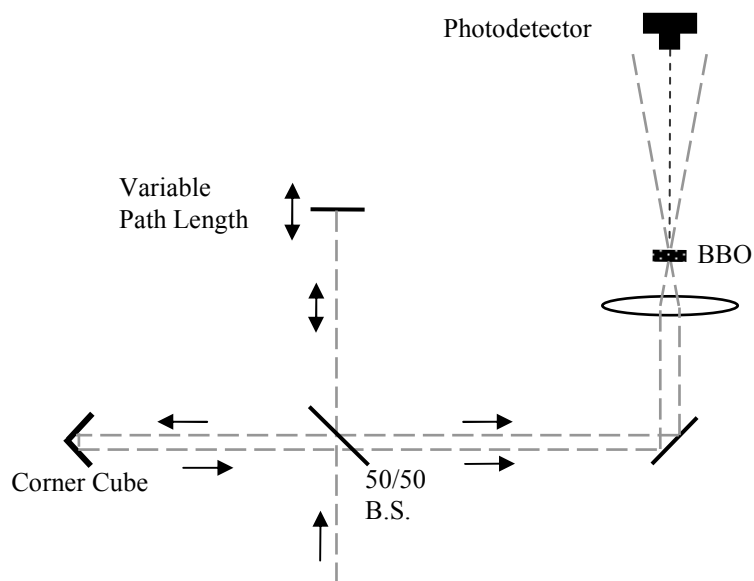


Fig 1.12: Intensity Autocorrelation Arrangement

The autocorrelator is shown in fig. 1.12. It has a similar arrangement to a Michelson interferometer, but one path is sent through a corner-cube retroreflector. This reflects the beam parallel to its incident path, but offset to one side. The two output beams are parallel but offset from each other. One path length is adjusted with a transducer rather than a track, which speeds up the sampling rate. They are focused to a single point in a nonlinear crystal (BBO in our lab), where frequency doubling occurs. After the lens, light doubled from each individual beam walks away from the center path, but light which results from mixing of the two beams will travel straight along the lens axis due to momentum conservation. The power of this beam is measured with a photodiode.

When there is no temporal overlap of the two pulses, there will be no inter-beam mixing, and the signal is zero. As the pulses overlap increases, the central beam power becomes stronger.

The combined electric field is  $E_T(t) = E(t) + E(t + \tau)$ ; when mixed, the strength of the second harmonic terms is proportional to the squared field,

$$P \propto E_T(t)^2 = E(t)^2 + E(t + \tau)^2 + 2E(t)E(t + \tau) \quad (1.3.5)$$

The first two terms propagate to the left and right of the central beam and are not recorded. The final term produces the beam which is sent to the photodiode. The photodiode response is much slower than the pulse duration, so the recorded signal is

$$S \propto \int_{-\infty}^{\infty} dt |E(t)E(t + \tau)|^2 = \int_{-\infty}^{\infty} dt |E(t)|^2 |E(t + \tau)|^2 \quad (1.3.6)$$

which is defined as the intensity autocorrelation. This signal is useful for finding the duration of ultrashort pulses. For a Gaussian pulse given by

$$|E(t)|^2 = \exp[-at^2] \quad (1.3.7)$$

The FWHM duration is

$$t_{FWHM} = 2\sqrt{\frac{\ln 2}{a}} \quad (1.3.8)$$

The signal in the autocorrelator is

$$S \propto \frac{\pi}{\sqrt{2a}} \exp\left[-\frac{a\tau^2}{2}\right] \quad (1.3.9)$$

which is a gaussian pulse with FWHM longer than  $t_{FWHM}$  by a factor of  $\sqrt{2} \approx 1.41$ .

By measuring the signal strength vs. delay, one can estimate the optical pulse duration.

### 1.3.2 Electro-Optic Sampling

A second technique we've employed to measure THz pulses is electro-optic sampling. In this method, the pulse to be sampled induces a birefringence in a nonlinear crystal. This birefringence is detected by passing a short optical probe through the crystal and measuring the change in its polarization. By varying the delay between the THz pulse and optical probe, the THz electric field can be mapped out as a function of time.

### 1.3.3 The Index Ellipsoid and the Pockels Effect

The Pockels effect is a nonlinear optics effect in which the index of refraction of a material changes linearly with an applied field. In an isotropic medium, the relationship between the electric and displacement fields is

$$D = \epsilon E \quad (1.3.10)$$

where  $\epsilon$  is the dielectric permeability. In an anisotropic medium, the permeability becomes a tensor,

$$D_i = \epsilon_{ij} E_j \quad (1.3.11)$$

Assuming a lossless medium, the permeability tensor is real and symmetric. It can therefore be diagonalized by finding the principal axes. In the basis of those principal axes, we have the three equations,  $D_i = \epsilon_{ii} E_i$ , where  $n_i = \sqrt{\epsilon_{ii}}$  is the refractive index for light polarized along each axis. To find the influence of the THz field on an

optical pulse, one needs to find how the field influences the permeability tensor and then diagonalize it to find the fast and slow axes.

It is typical to treat the impermeability rather than the permeability tensor, defined as the inverse,

$$\eta_{ij} = (\varepsilon^{-1})_{ij} \quad (1.3.12)$$

The impermeability tensor is often used because the index ellipsoid describing the refractive index of the material can be written

$$\sum_{ij} R_i \eta_{ij} R_j = \frac{x^2}{n_x^2} + \frac{y^2}{n_y^2} + \frac{z^2}{n_z^2} + \frac{xy}{n_{xy}^2} + \frac{yz}{n_{yz}^2} + \frac{zx}{n_{zx}^2} = 1 \quad (1.3.13)$$

In a basis where the impermeability tensor is diagonalized, the last three terms vanish.

Now consider an impermeability tensor which depends on an applied electric field. The slowly-varying THz field plays the role of this applied field. Expanding the tensor in the field, we have

$$\eta_{ij}(E) \approx \eta_{ij}^{(0)} + \sum_k r_{ijk} E_k \quad (1.3.14)$$

where the  $\eta_{ij}^{(0)}$  and  $r_{ijk}$  are specific to the crystal structure.

Zinc telluride has a zincblende structure, which is isotropic when no field is applied ( $n_1 = n_2 = n_3$ ). Additionally, all  $r_{ijk}$  are zero except for the six identical elements  $r \doteq r_{231} = r_{321} = r_{132} = r_{312} = r_{123} = r_{213}$ . The index ellipsoid becomes

$$\sum_{ij} R_i \left( \eta_{ij}^{(0)} + \sum_k r_{ijk} E_k \right) R_j = \frac{x^2}{n_0^2} + \frac{y^2}{n_0^2} + \frac{z^2}{n_0^2} + 2r (E_x yz + E_y zx + E_z xy) \quad (1.3.15)$$

To maximize electro-optic effects, our ZnTe crystals are cut normal to the  $[110]$  crystal axis. I therefore introduce a basis in which  $\hat{x}$  points in the  $[-1,1,0]$  direction,  $\hat{y}$  points in the  $[0,0,1]$  direction, and  $\hat{z}$  points in the  $[1,1,0]$  direction.

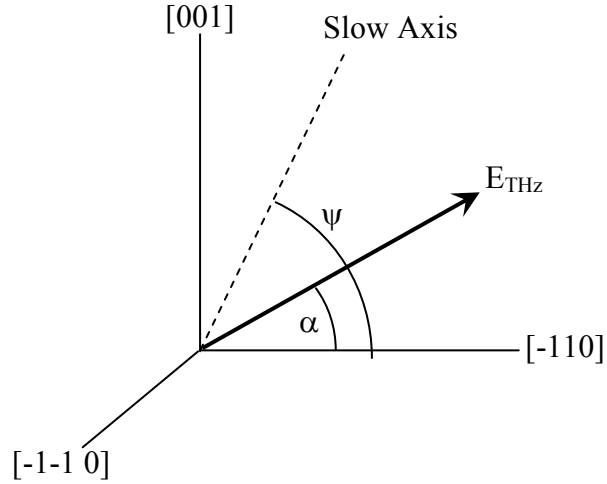


Fig 1.13: THz Polarization in an Electro-Optic Crystal.

As shown in fig. 1.13, let the THz field  $E_{\text{THz}}$  propagate in the  $\hat{z}$  direction, such that its polarization is at an angle  $\alpha$  from the  $\hat{x}$  direction. By diagonalizing the impermeability tensor in this basis, the principal axes can be found to be [19]

$$P_1 = \frac{1}{2} \sqrt{1 + \frac{\sin(\alpha)}{\sqrt{1 + 3 \cos^2(\alpha)}}} \begin{pmatrix} -1 \\ +1 \\ \frac{2\sqrt{2} \cos(\alpha)}{\sqrt{1 + 3 \cos^2(\alpha) + \sin(\alpha)}} \end{pmatrix} \quad (1.3.16)$$

$$P_2 = \frac{1}{2} \sqrt{1 - \frac{\sin(\alpha)}{\sqrt{1 + 3 \cos^2(\alpha)}}} \begin{pmatrix} +1 \\ -1 \\ \frac{2\sqrt{2} \cos(\alpha)}{\sqrt{1 + 3 \cos^2(\alpha)} - \sin(\alpha)} \end{pmatrix} \quad (1.3.17)$$

$$P_3 = \begin{pmatrix} -1 \\ -1 \\ 0 \end{pmatrix} \quad (1.3.18)$$

$P_1$  and  $P_2$  are in the plane  $\hat{x} \times \hat{y}$ ,  $P_1$  making an angle  $\psi$  with the  $\hat{x}$  direction given by

$$\cos(2\psi) = \frac{\sin(\alpha)}{\sqrt{1 + 3 \cos^2(\alpha)}} \quad (1.3.19)$$

Under the approximation  $rE \ll \frac{1}{n_0^2}$  the principal refractive indices are

$$n_1 = n_0 + \frac{n_0^3 rE}{4} \left( \sin(\alpha) + \sqrt{1 + 3 \cos^2(\alpha)} \right) \quad (1.3.20)$$

$$n_2 = n_0 + \frac{n_0^3 rE}{4} \left( \sin(\alpha) - \sqrt{1 + 3 \cos^2(\alpha)} \right) \quad (1.3.21)$$

$$n_3 = n_0 - \frac{n_0^2 rE}{2} \sin(\alpha) \quad (1.3.22)$$

A THz pulse passing through a ZnTe crystal will induce this birefringence. If a short optical pulse is passed through the crystal, it can sample the THz field as they co-propagate. Projecting the optical pulse along the fast and slow axes, the relative phase shift between the two components is given by

$$\Gamma(\alpha) = \frac{\omega_o}{c} (n_2 - n_1) d = \frac{\omega_o d}{2c} n_0^2 r E_{THz} \sqrt{1 + 3 \cos^2(\alpha)} \quad (1.3.23)$$

where  $\omega_o$  is the optical pulse frequency,  $d$  the thickness of the crystal, and  $c$  the speed of light. This will make the probe beam slightly elliptic, by an amount proportional to the THz field. This birefringence is maximized for  $\alpha = 0^\circ$ , where the THz field lies along the  $\hat{x} = [-110]$  direction. In this situation,  $\psi = 45^\circ$ , so the effect on the probe beam is maximized with the probe beam's polarization either  $0^\circ$  or  $90^\circ$  from the THz polarization.

### 1.3.4 Ellipsometry of the THz beam

A typical arrangement for sampling the THz pulse is shown in fig. 1.14:

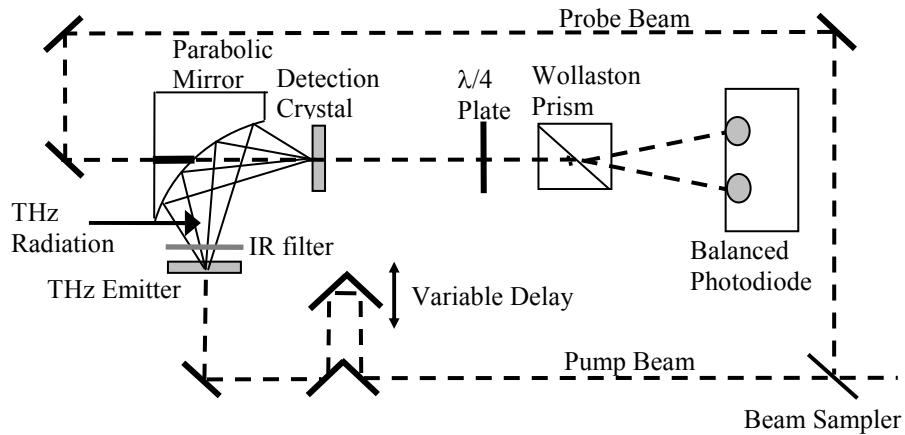


Fig 1.14: Electro-Optic Sampling Arrangement. The input beam is an 800 nm, 90 fs pulse from a mode-locked laser.

The THz pulse induces a birefringence in the ZnTe detector crystal. The optical probe beam passes through the detector and acquires a slight ellipticity. It is then passed through a quarter-wave plate where it becomes almost circularly polarized (for  $E_{\text{THz}} = 0$ , the wave is exactly circular). It is then passed through a Wollaston prism, which is a cube polarizer that separates the horizontal and vertical components. The power in these two components is measured using two photodetectors, and the difference between them measured.

To calculate the effect of the THz field, I consider a maximum signal situation where  $\alpha = 0$  and  $\psi = 45^\circ$ . This corresponds to the THz field pointing in the  $\hat{x}$  direction, with the fast axis of the induced birefringence  $45^\circ$  from this. It is important to note

that even though the index of refraction along the principal axes depends on the field strength, the direction does not. To maximize the effect on the probe beam, it will be polarized in the  $\hat{x}$  direction as well.

The incoming optical beam's polarization is

$$\vec{P}_o = \begin{pmatrix} 1 \\ 0 \end{pmatrix} \quad (1.3.24)$$

corresponding to the  $\hat{x}$  direction. Projecting this on the fast and slow axes, which are rotated by  $45^\circ$ ,

$$\vec{P}_o = \frac{1}{\sqrt{2}} \begin{pmatrix} \frac{1}{\sqrt{2}} \\ \frac{1}{\sqrt{2}} \end{pmatrix} + \frac{1}{\sqrt{2}} \begin{pmatrix} \frac{1}{\sqrt{2}} \\ -\frac{1}{\sqrt{2}} \end{pmatrix} \quad (1.3.25)$$

A relative phase shift of  $\Gamma$  is introduced to one of the axes by the birefringence,

$$\vec{P}_o = \frac{1}{\sqrt{2}} \begin{pmatrix} \frac{1}{\sqrt{2}} \\ \frac{1}{\sqrt{2}} \end{pmatrix} + \frac{e^{-i\Gamma}}{\sqrt{2}} \begin{pmatrix} \frac{1}{\sqrt{2}} \\ -\frac{1}{\sqrt{2}} \end{pmatrix} \quad (1.3.26)$$

In addition, the probe beam is sent through a quarter-wave plate, adding an additional  $\frac{\pi}{4}$  phase shift.

$$\vec{P}_o = \frac{1}{\sqrt{2}} \begin{pmatrix} \frac{1}{\sqrt{2}} \\ \frac{1}{\sqrt{2}} \end{pmatrix} + \frac{e^{-i(\Gamma+\frac{\pi}{4})}}{\sqrt{2}} \begin{pmatrix} \frac{1}{\sqrt{2}} \\ -\frac{1}{\sqrt{2}} \end{pmatrix} \quad (1.3.27)$$

Projecting the probe beam back in the  $\hat{x}$  and  $\hat{y}$  directions;

$$|P_{ox}| = |\langle x | P_0 \rangle| = \left| (1 \ 0) \begin{pmatrix} \frac{1}{2} + \frac{e^{-i(\Gamma + \frac{\pi}{4})}}{2} \\ \frac{1}{2} - \frac{e^{-i(\Gamma + \frac{\pi}{4})}}{2} \end{pmatrix} \right| \quad (1.3.28)$$

$$= \left| \frac{1}{2} \left( 1 + e^{-i(\Gamma + \frac{\pi}{4})} \right) \right| = \cos \left( \Gamma + \frac{\pi}{4} \right) = \frac{1}{\sqrt{2}} (\cos \Gamma - \sin \Gamma) \quad (1.3.29)$$

and

$$|P_{oy}| = |\langle y | P_0 \rangle| = \left| (0 \ 1) \begin{pmatrix} \frac{1}{2} + \frac{e^{-i(\Gamma + \frac{\pi}{4})}}{2} \\ \frac{1}{2} - \frac{e^{-i(\Gamma + \frac{\pi}{4})}}{2} \end{pmatrix} \right| \quad (1.3.30)$$

$$= \left| \frac{1}{2} \left( 1 - e^{-i(\Gamma + \frac{\pi}{4})} \right) \right| = \sin \left( \Gamma + \frac{\pi}{4} \right) = \frac{1}{\sqrt{2}} (\sin \Gamma + \cos \Gamma) \quad (1.3.31)$$

Assuming a small phase shift  $\Gamma$ ,

$$|P_{ox}| \approx \frac{1}{\sqrt{2}} (1 - \Gamma) \quad (1.3.32)$$

$$|P_{oy}| \approx \frac{1}{\sqrt{2}} (1 + \Gamma) \quad (1.3.33)$$

For zero THz field, the optical polarization is circular, and the power for horizontal and vertical linear polarizations is the same. The difference is zero in this case. For a nonzero THz field, the difference between the two component powers is

$$S = |P_{oy}|^2 - |P_{ox}|^2 \approx \frac{1}{2} (1 + 2\Gamma) - \frac{1}{2} (1 - 2\Gamma) = 2\Gamma \quad (1.3.34)$$

Since the relative phase shift is proportional to  $E_{\text{THz}}$ , the difference signal is proportional to the THz field. As the relative delay between pump and probe is varied, this difference signal is recorded, yielding the THz field strength as a function of time.

In practice, this difference signal is fairly weak, so a lock in amplifier is used to boost and filter the signal. An optical chopper is placed in the optical pump beam which modulates that beam with a frequency of 200-1000 Hz. We use a Stanford Research Systems lock-in amplifier to record and digitize the signal from a balanced photodiode. The lock-in amplifier multiplies the signal by a sine and cosine wave with the same frequency as the chopper. Since sinusoids of different frequencies are orthogonal, only the modulation frequency is amplified, and noise at other frequencies is filtered out.

## 2. Generation of Shaped, Multiple-Cycle THz Pulses in PPLN

### 2.1 Narrowband THz Generation in PPLN

Optical rectification in ZnTe is sufficient to create a short, single-cycle THz pulse. This is useful for some studies, such as broadband THz spectroscopy and investigating exciton dynamics in semiconductor nanostructures. One can extend the utility of THz spectroscopy by generating other pulses. In the following, I describe our work on creating shaped, multiple-cycle pulses in lithium niobate (LiNbO<sub>3</sub>).

To create multiple-cycle pulses, we use crystals of periodically-poled LiNbO<sub>3</sub>, commonly denoted PPLN. The nonlinear effect used in THz generation is optical rectification, just as in ZnTe. In LiNbO<sub>3</sub>, the THz refractive index is  $n_{\text{THz}} = 5.3$ , while the optical refractive index is  $n_o = 2.9$ . Because of this, the THz frequency radiation moves slower through the crystal than the optical pump pulse creating it. If it travels sufficiently far through the crystal, the THz emission created at later parts of the crystal interferes destructively with the emission at earlier parts of the crystal. For unpatterned LiNbO<sub>3</sub>, this will suppress THz generation. An estimate of the distance required for the THz to begin interfering with itself is the walk-off length,

$$l_w = \frac{c\tau}{n_{\text{THz}} - n_o} \quad (2.1.1)$$

where  $\tau$  is the optical pulse duration. For a pulse duration of 100 fs,  $n_{\text{THz}} = 5.3$  and  $n_o = 2.9$ , the walk-off length is 125 microns.

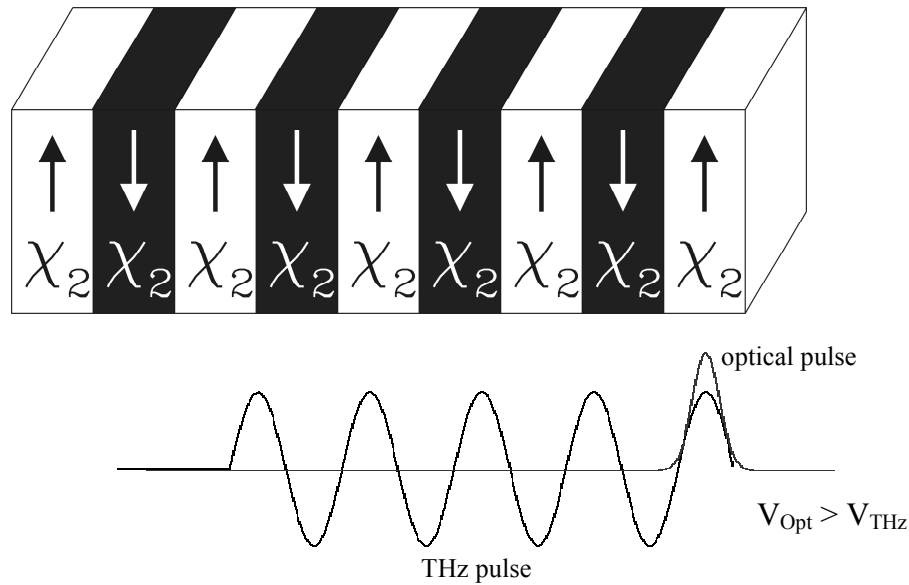


Fig 2.1: Periodically-Poled Lithium Niobate. As the optical driving pulse passes through the crystal, it leaves a THz “trail” behind it.

By patterning the  $\text{LiNbO}_3$ , quasi-phase matching can be achieved. As shown in fig. 2.1, the crystal’s poling is reversed periodically with a spatial period comparable to the walk-off length. Reversing the poling has the effect of reversing the direction of  $\chi^{(2)}$ , which reverses the direction of the rectified polarization. As the pump pulse traverses each domain, a THz half-cycle is created, which falls behind as the pump enters the next domain. After traversing the length of the PPLN, a trail of THz half-waves is left behind, effectively making a narrow-band, multicycle pulse.

The emitted THz wavelength can be calculated by using the difference in group velocities of the two pulses. For a  $\text{LiNbO}_3$  crystal, after crossing a domain width  $d$ , the optical pulse leads the THz pulse by a distance

$$\frac{\lambda_{THz}}{2} = d \left( 1 - \frac{v_{THz}}{v_o} \right) = d \left( 1 - \frac{n_o}{n_{THz}} \right) \quad (2.1.2)$$

corresponding to a half-wavelength of the THz pulse. The frequency associated with this wavelength is

$$f_{THz} = \frac{v_{THz}}{2d \left( 1 - \frac{n_o}{n_{THz}} \right)} = \frac{c}{2d(n_{THz} - n_o)} \quad (2.1.3)$$

In PPLN, a 1 THz emission (300  $\mu\text{m}$ ) would be given by a crystal with domain length 62.5 microns.

Ideally one would like a tunable source for multicycle pulses. To achieve this, one can use the fan-out structure (fig. 2.2).

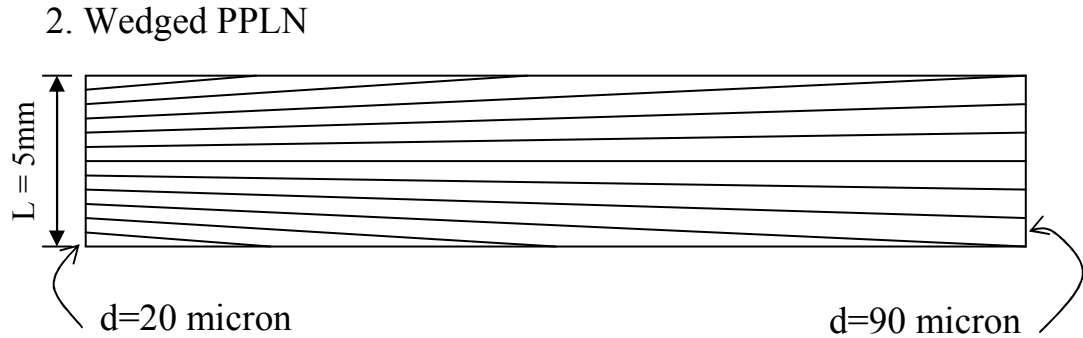


Fig 2.2: Fanned out PPLN. The domain thickness increases as the driving beam is swept across the crystal from left to right.

To create THz of a specific frequency, the pump beam is focused onto an area much smaller than the crystal face. As the beam is swept across the face, it creates THz with a frequency determined by its vertical position. This is shown in fig. 2.3.

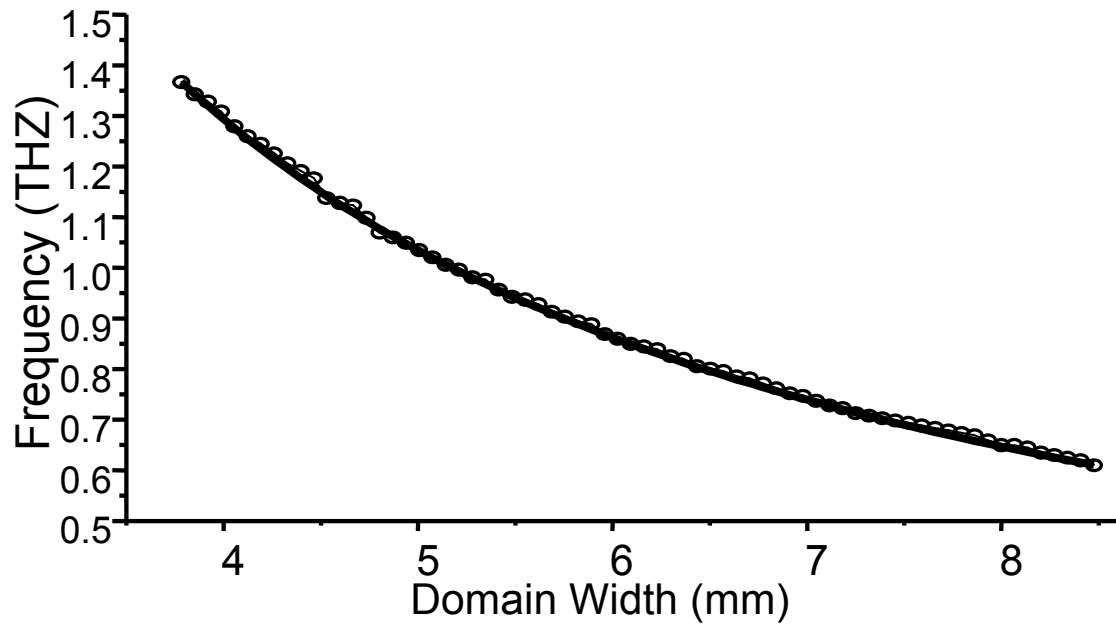


Fig 2.3: THz frequency vs. Domain Width. The circles represent measured values, the solid line is calculated [2].

## 2.2 Shaping THz pulses emitted by FO-PPLN

Since each region of the fanned-out PPLN emits a different THz frequency, it becomes possible to create a number of different frequencies and recombine them. An arrangement for doing this is shown in fig.2.4:

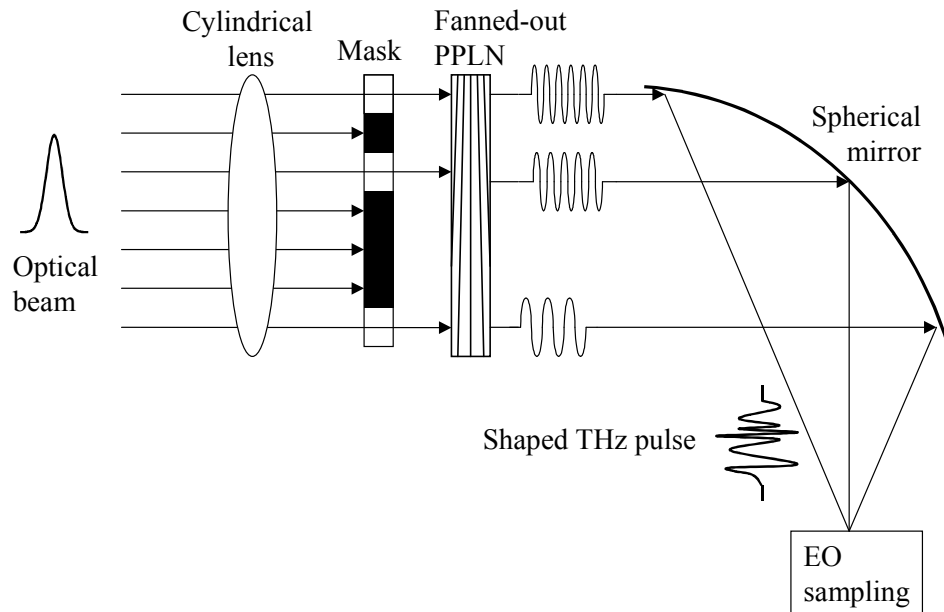


Fig 2.4: Pulse Shaping Arrangement. Various regions of the FO-PPLN are masked off, suppressing THz frequencies emitted from those regions.

The driving pulse for the arrangement comes from a 76 MHz Ti:Sapphire mode-locked laser operating at 800nm with a bandwidth of 14nm. The pulse duration of the laser was  $\sim 100$  fs, and its output is about 1W, giving a pulse energy of 13 nJ. This was amplified in a Ti:Sapphire regenerative amplifier which also had an output of 1 W, but operated at a repetition rate of 1 KHz, giving a pulse energy of  $\sim 1$ mJ. The output spectrum of the regenerative amplifier matched the output spectrum of the mode-locked laser.

The fanned-out PPLN used in the experiment contained domain widths ranging from 40 microns at one end to 100 microns at the other; so that the emitted THz frequency was continuously tunable from 0.6 THz to 1.5 THz.

The driving beam was brought to a line focus using a 10 cm cylindrical lens. This illuminated a long line across the PPLN face, so that the THz output would consist of many THz frequency components.

After the PPLN, the optical driving beam is filtered out using a piece of polyethylene. The THz beam is collected using a spherical mirror. The advantage of the spherical mirror over a parabolic mirror is that a spherical mirror has a different focal length in the vertical and horizontal directions. The vertical focal length is given by  $f_v = R/(2\cos\theta)$  and the horizontal by  $f_h = (R\cos\theta)/2$ ; where  $\theta$  is the incident angle. Because the two beam axes have two different focuses, we can compensate for the cylindrical focus used to make a line. The THz beam is collected in this way and sent to an electro-optic sampling arrangement and the THz electric field recorded as a function of time. The waveforms are measured with 0.1-ps time step and 80-ps time window, which gives the spectral resolution of 0.0125 THz.

The spectrum of the PPLN's output is shown in fig 2.5a. It is notable that the spectrum does not have a smooth profile. There are a number of water absorption lines in this region which suppress certain frequencies. Additionally, the PPLN crystal used in the experiment had some previous damage which led some regions to be less emissive than others. However, its output was sufficient to demonstrate pulse-shaping.

To this end, a metal mask was placed in the optical beam just before the crystal. This mask allowed some parts to emit THz and suppressed that emission from others.

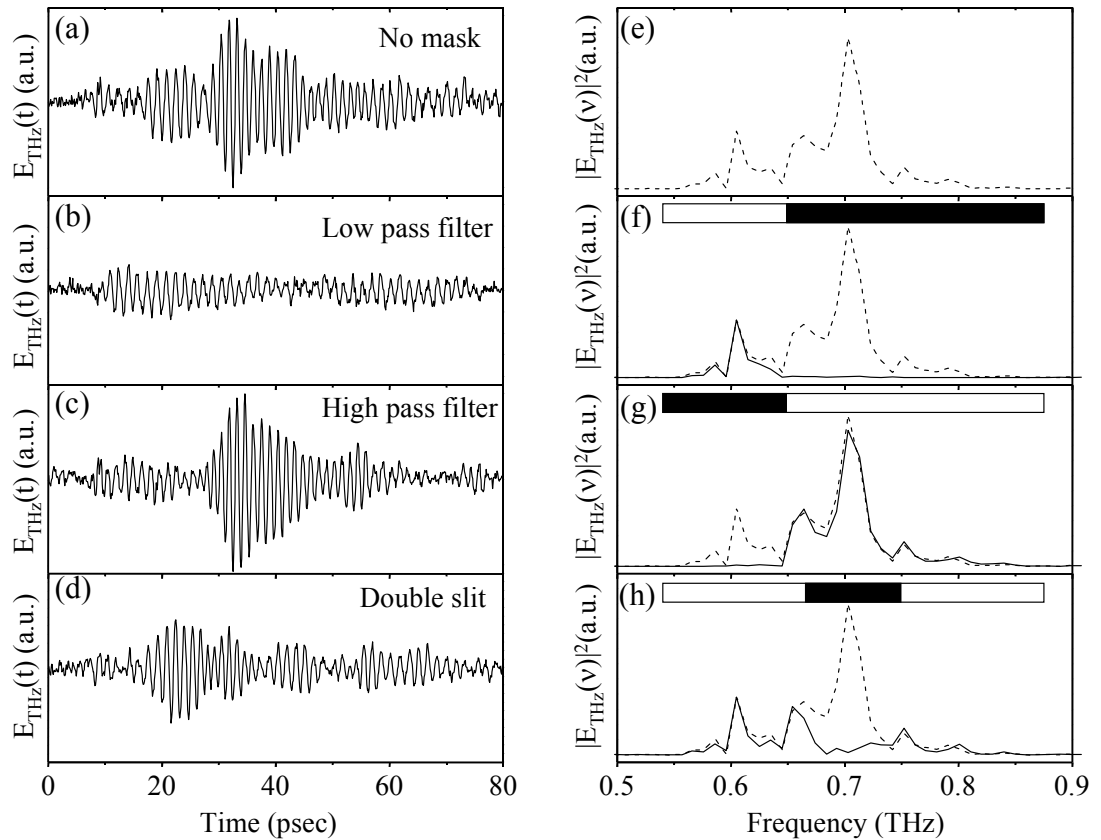


Fig 2.5: Spectral Filtering of FO-PPLN Output. The black region of the bar above each spectrum represents the crystal region that was masked off. The dashed curve in each spectrum is the unmasked spectrum [1].

Fig. 2.5 shows the frequency filtered data. In each spectrum, a bar at the top indicates what sections of the PPLN were illuminated. In the second spectrum, frequencies higher than 0.65 THz were blocked, forming a low-pass filter. The emitted spectrum is narrower, and the time-domain recording reflects this, showing a fairly long, narrowband pulse. In the third spectrum, frequencies lower than 0.64 THz were blocked, forming a high-pass filter. In this case, most of the THz spectrum is present, and though there are some differences between this spectrum and the full spectrum, the two are quite similar to the eye. In the last spectrum, the central part of

the spectrum from 0.55 to 0.85 THz is blocked. In the accompanying time-domain image, there is a noticeable beat with a period  $\sim 10$  ps. This is consistent with the higher ( $\sim 0.75$  THz) and lower ( $\sim 0.65$  THz) parts of the THz spectrum combining to form a beat frequency ( $\sim 0.1$  THz). For the high-pass and low-pass spectra the cutoff is quite abrupt. The double-slit arrangement in the fourth spectrum does not share this, but instead appears somewhat noisy. In fact, the larger portion of the spectral power has been removed by blocking the center of the beam, so the signal was significantly weaker. As a result, the signal-to-noise ratio is much worse for that filter.

This demonstrates that a fanned-out PPLN can be used to create a shaped THz pulse. Different regions of the crystal can be made to emit, and the spatially separated components recombined to make the composite pulse. For complete control over the pulse shape, one could incorporate a MEMS mirror, consisting of an array of very small movable mirrors. This would allow one to add a phase delay to the different components before reassembly. Using a programmable filter for the spatial filtering and a MEMS mirror for phase control, one could completely control the shape of the THz pulse during the course of an experiment.

### 3. Creating Multiple-Cycle Pulses through Difference-Frequency Generation

We have developed a simple method for creating multi-cycle, narrowband THz pulses. It is similar to our other THz generation techniques in that it uses a second order  $\chi^{(2)}$  effect in a nonlinear crystal. Rather than rectifying an optical pulse, as is done in the previous methods described, we use frequency mixing of light with two slightly different frequencies.

Frequency mixing to produce THz is not a new idea. In 1965 Zernike and Berman demonstrated the method using a pulsed neodymium glass laser [21], and later Brown *et al.* produced THz mixing CW lasers on a photoconductive antenna [22].

To do dynamic studies of systems with THz pulses, one would like to use a femtosecond laser to generate them. This allows high-resolution pump-probe studies to be performed. In 1996 Weling and Austin introduced a technique in which chirped ultrashort pulses were mixed in a PC antenna [23]. While this technique was tunable and could be used in pump-probe studies, it suffered from a frequency spectrum limited by the carrier relaxation time to signals less than 800 GHz. Additionally, PC antennas saturate at a lower fluence than nonlinear processes, so a method incorporating nonlinear crystals could give higher THz energies.

### 3.1 Difference Frequency Generation Using Chirped Pulses

#### 3.1.1 Difference Frequency Generation

Consider an electric field with two frequency components,

$$\vec{E} = \vec{E}_0 [\exp(-i\omega_1 t) + \exp(-i\omega_2 t) + c.c.] \quad (3.1.1)$$

When inserted into the second-order term for a material's polarization, that term becomes

$$\begin{aligned} P_i^{(2)} &= \frac{1}{2} \chi_{ijk}^{(2)} E_{0j} E_{0k} [\exp(-i\omega_1 t) + \exp(-i\omega_2 t) + c.c.]^2 \\ &= \frac{1}{2} \chi_{ijk}^{(2)} E_{0j} E_{0k} \{ \exp[-i2\omega_1 t] + \exp[-i2\omega_2 t] + 2 \exp[0] \\ &\quad + \exp[-i(\omega_1 + \omega_2)t] + \exp[-i(\omega_1 - \omega_2)t] + c.c. \} \end{aligned} \quad (3.1.2)$$

The last two terms represent sum and difference frequency generation (DFG and SFG). Using a laser operating at 800nm, a 1 THz emission corresponds to a difference of 2 nm. Since a mode-locked femtosecond laser typically has a bandwidth between 11 and 14 nm, this suggests that a single laser pulse could be used as the source for both frequencies. To do so, we introduce a linear chirp into the probe beam.

### 3.1.2 The Chirped Pulse

A linearly chirped pulse (shown in fig 3.1) can be written as

$$E(t) = E_0 \exp[-at^2] \exp[-i(\omega_0 + bt)t] \quad (3.1.3)$$

where  $\omega_0$  is the central angular frequency,  $\tau_p = \sqrt{2 \ln 2 / a}$  is the pulse duration, and

$b$  is the chirp parameter. The instantaneous angular frequency is

$$f_{ins}(t) = \frac{d\phi}{dt} = \omega_0 + 2bt \quad (3.1.4)$$

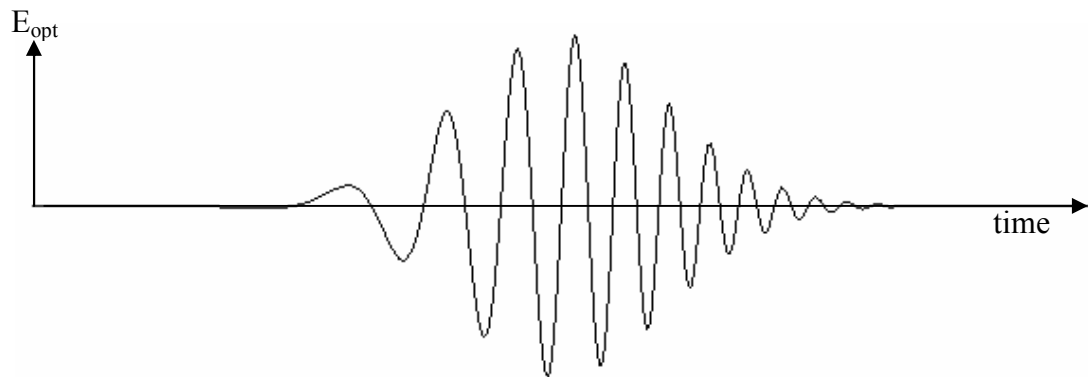
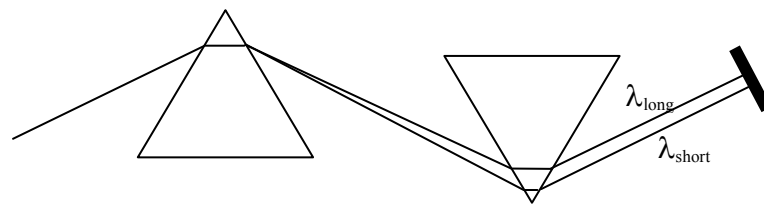
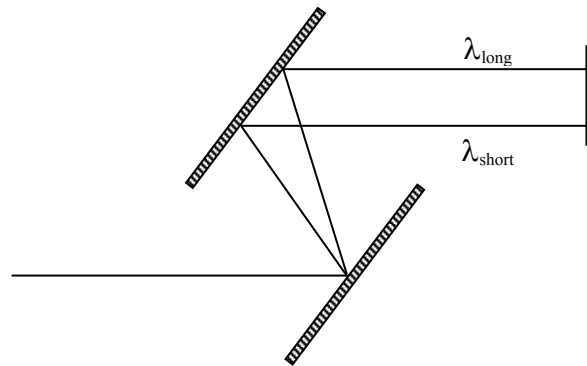


Fig 3.1: The Chirped Pulse.

There are a number of ways to create a chirped pulse. Typically, a beam is passed through a set of prisms or diffraction gratings so that lower frequency components of a pulse travel a longer distance than higher frequency components, or vice versa. This introduces a group delay dispersion along the optical path; the pulse will become elongated in time, and acquire a chirp. Example methods for introducing a chirp are shown in fig. 3.2.



Prism Arrangement



Diffraction Grating

Fig 3.2: Group Velocity Dispersion Arrangements. Above is a double-pass prism pair, which forms a four prism arrangement. The beam enters from the left, passes through the prisms and is reflected back by a mirror. Importantly, longer wavelength components of the pulse travel a different distance than shorter wavelengths. The second arrangement is a pair of diffraction gratings, again in a double-pass configuration. In this case, longer wavelength components travel a farther distance.

For a linearly chirped pulse, the instantaneous frequency varies linearly with time. If we should mix earlier parts of the pulse with later parts, there will be a difference-frequency which will result in DFG. Specifically, we split the pulse into two, add a delay to one path by a time  $\tau$  and recombine them. Then the difference between the central frequencies of the two pulses is

$$\begin{aligned}\Delta f &= \frac{\Delta\omega}{2\pi} = \frac{1}{2\pi}(\omega(t+\tau) - \omega(t)) \\ &= \frac{b\tau}{\pi}\end{aligned}\tag{3.1.5}$$

By passing the recombined pulses through a nonlinear crystal such as ZnTe, a field with frequency  $\Delta f$  will be created.

### 3.1.3 Pulse Splitter and Recombiner

Fig 3.2 shows the arrangement for the pulse splitter:

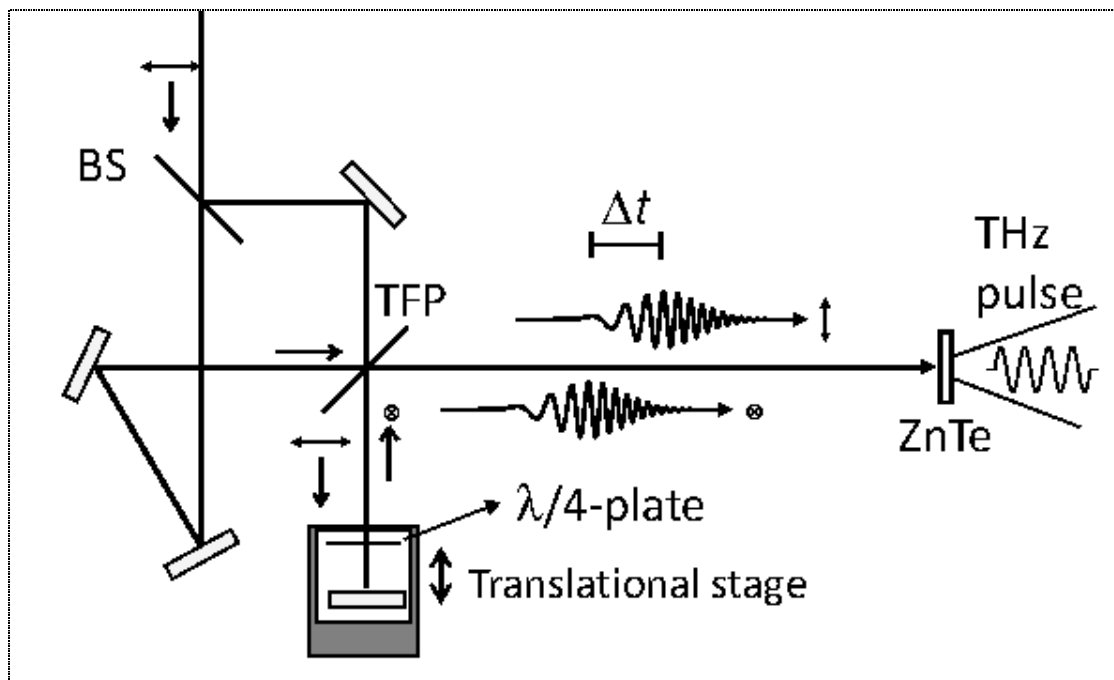


Fig 3.3: Pulse Delay Arrangement

All the optics used were optimized for infrared light with wavelength close to  $800\ \mu\text{m}$ . The beam is initially *s*-polarized. It is split with a 50-50 beam splitter into two paths. The thin film polarizer (TFP) is chosen such that it transmits *s*-polarization (horizontal) and reflects *p*-polarization (vertical) at a certain angle –  $53^\circ$  in this case. One path is reflected from two mirrors and passed through the *s*-polarizer unchanged. The second path passes through the TFP once and is sent through a quarter wave plate. It is reflected from a mirror back through the quarter-wave plate and towards the TFP. Passing through a quarter-wave plate twice is the same as passing through a half-wave plate once, and that beam is then reflected from the TFP. The recombined beams travel out of the arrangement collinearly.

Since the recombined beams are orthogonally polarized, they will mix through type II generation in a nonlinear crystal (ZnTe in our arrangement). Alternatively, one could use a simple Michelson interferometer to split and recombine the beams with the same polarization. The disadvantage to the latter is that 50% of the input power is necessarily lost, an undesirable outcome. Additionally, ZnTe exhibits parasitic effects at high fluence such as two-photon absorption and carrier generation. These effects are minimized for light polarized in the [001] direction [19], but that direction also gives the least DFG, just as for optical rectification. In a type II arrangement, one beam will be polarized in the [001] direction, reducing the total parasitic effects. Type II becomes slightly more efficient due to the anisotropy of third-order generation in ZnTe.

### 3.1.4 Angular Dependence of the Emission

To calculate the angular dependence of the DFG emission, I examine the factor

$$P_i^{(2)} = \frac{1}{2} \chi_{ijk}^{(2)} E_{0j} E_{0k} \quad (3.1.6)$$

from eq. 1.2.2. In the crystal frame, the orthogonal field polarizations are given by

$$\vec{E}_1 = \hat{z} \cos \theta + \frac{1}{\sqrt{2}} (-\hat{x} + \hat{y}) \sin \theta \quad (3.1.7)$$

and

$$\vec{E}_2 = \hat{z} \sin \theta + \frac{1}{\sqrt{2}} (-\hat{x} + \hat{y}) \cos \theta \quad (3.1.8)$$

Returning to the d-matrix,

$$\begin{pmatrix} P_x \\ P_y \\ P_z \end{pmatrix} = 2\varepsilon_0 d_{14} \begin{pmatrix} 0 & 0 & 0 & 1 & 0 & 0 \\ 0 & 0 & 0 & 0 & 1 & 0 \\ 0 & 0 & 0 & 0 & 0 & 1 \end{pmatrix} \cdot E_0 \begin{pmatrix} \frac{1}{2} \cos \theta \sin \theta \\ \frac{1}{2} \cos \theta \sin \theta \\ \cos \theta \sin \theta \\ (\cos^2 \theta + \sin^2 \theta) \\ -(\cos^2 \theta + \sin^2 \theta) \\ -2 \cos \theta \sin \theta \end{pmatrix} \quad (3.1.9)$$

after some algebra,

$$\begin{pmatrix} P_x \\ P_y \\ P_z \end{pmatrix} = 2\varepsilon_0 d_{14} E_0 \begin{pmatrix} \sqrt{2} \\ -\sqrt{2} \\ -2 \sin \theta \cos \theta \end{pmatrix} = -4\varepsilon_0 d_{14} E_0 \left[ \hat{z} \sin \theta \cos \theta + \frac{1}{\sqrt{2}} (-\hat{x} + \hat{y}) \right] \quad (3.1.10)$$

Neglecting the overall factors, the emitted power as a function of angle (fig. 3.4) is

$$\text{THz Power} \propto |\vec{P}|^2 \propto 1 + \cos^2(\theta) - \cos^4(\theta) \quad (3.1.11)$$

and the angle of polarization is given by

$$2 \tan \phi \cos 2\theta = 1 \quad (3.1.12)$$

in the crystal frame (fig. 3.4). In the lab frame, the crystal is rotated by an angle  $-\theta$  and the driving polarizations held constant, so the THz polarization in the lab should be  $\phi_L = \phi + \theta_L$ .

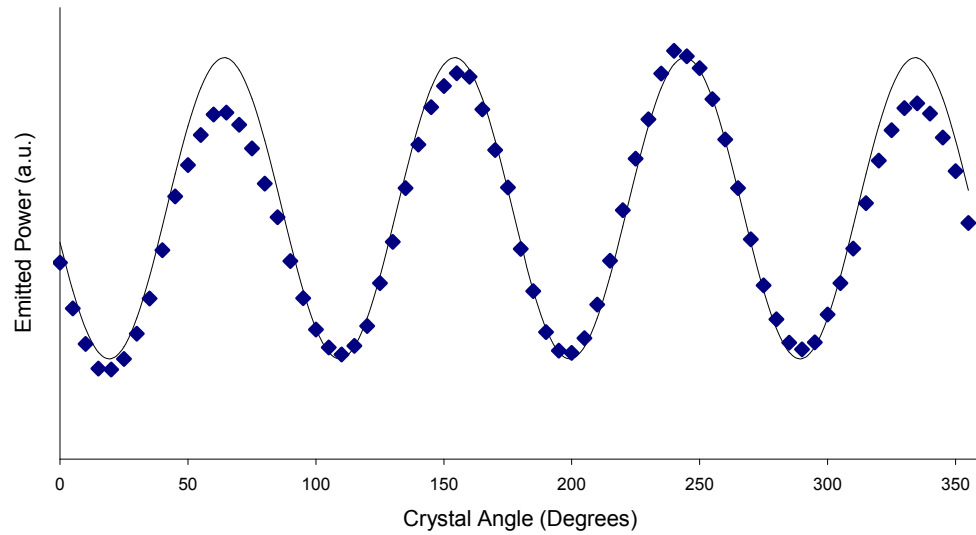


Fig. 3.4: THz Power vs. Angle. The solid line is the calculated THz emission for various crystal angles, the dots are the measured emission.

The angular dependence of this process is significantly different than that of optical rectification. As a result, the type II DFG process can be distinguished from rectification by rotating the crystal and observing the emitted THz power.

### 3.2 Experimental Arrangement

The laser source was our femtosecond mode-locked laser emitting at 800 nm with a 14 nm bandwidth. The pulse duration of this pulse was  $\sim 100$  fs. The pulse was then amplified by a regenerative amplifier (Legend by Coherent, Inc.) In the regenerative amplifier, the seed pulse is stretched in time by passing the beam through a pair of diffraction gratings. This lowers the peak power so that the pulse can be amplified without damaging the amplifying rod. At the same time, this induces an optical chirp in the pulse. After amplification, this chirping is reversed in another pair of gratings which recompresses the pulse. To introduce a chirp in the pump pulse, we adjusted the output compressor so that it didn't entirely compensate for the first grating pair.

We used a silicon bolometer to measure the THz radiation power. Taking into account the pulsed nature of our source, we applied a detector responsivity of  $9.26 \times 10^9$  V/J; or  $9.26 \times 10^6$  V/W with a 1-kHz repetition rate. This is about one tenth of the responsivity calibrated with CW sources. To measure the spectra of the emitted radiation, we built a THz Michelson interferometer using a Mylar beamsplitter and performed field autocorrelations. This arrangement is shown in Fig 3.3. While this method loses the phase information of the spectrum, it preserves the power spectrum of the pulse.

### 3.3 MEASUREMENTS

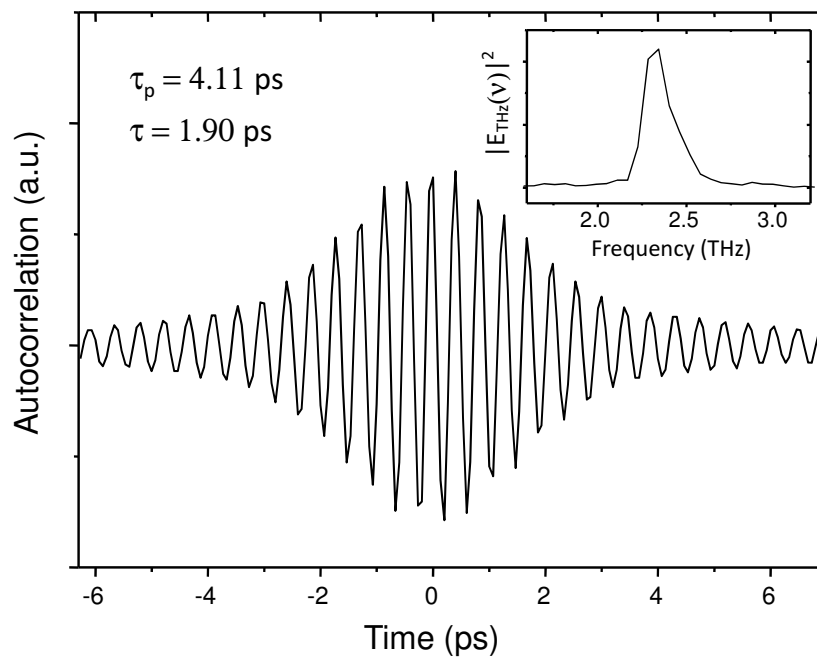


Fig. 3.5: Example THz Field Autocorrelation

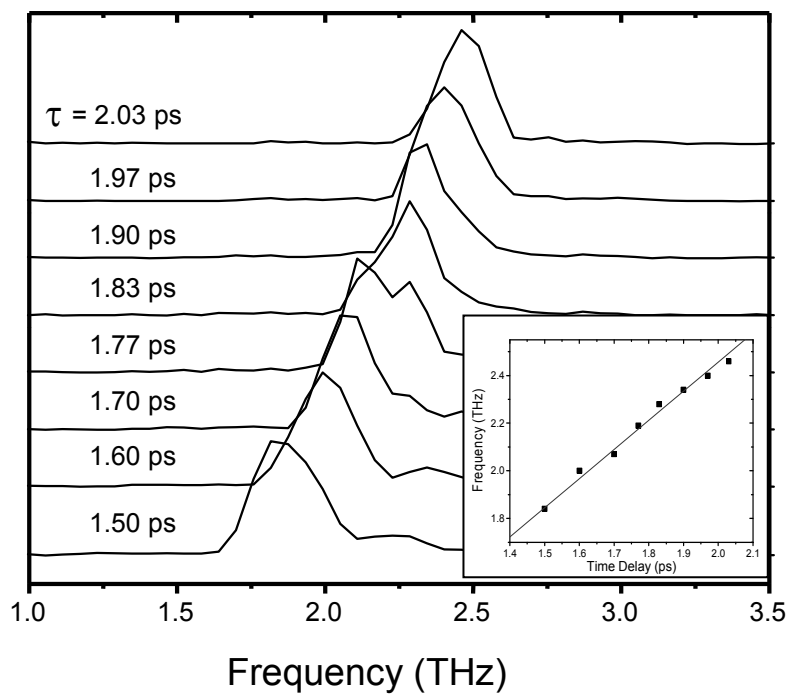


Fig 3.6: THz Spectrum vs. Pulse Delay. The numbers on the left show the delay used for the pulse splitter.

Fig 3.5 shows a typical THz-field autocorrelation and associated spectrum when the optical pulse duration and the time delay are 4.1 and 1.9 ps, respectively. The THz radiation is narrowband: the spectrum centered at 2.34 THz has a spectral width of  $\sim 0.2$  THz with an associated quality factor of  $\sim 11$ . The experimental setup is capable of fine and continuous tuning of frequency. Fig 3.6 shows a set of spectra of the THz radiation with central frequencies ranging from 1.8 and 2.5 THz. The water absorption lines near 2.2 THz are visible. For this measurement, the optical pulse duration is held constant at 4.11 ps, and the time delay between the two pulses are varied from 1.50 to 2.03 ps. The frequency of the THz radiation varies linearly with pulse delay as shown in the inset of Fig. 3.6. The solid line is the best linear fit to the data, which leads to the chirp parameter  $b = 3.85 \text{ ps}^{-2}$  using  $\Delta f = b\tau/\pi$  from eq. 3.1.5.

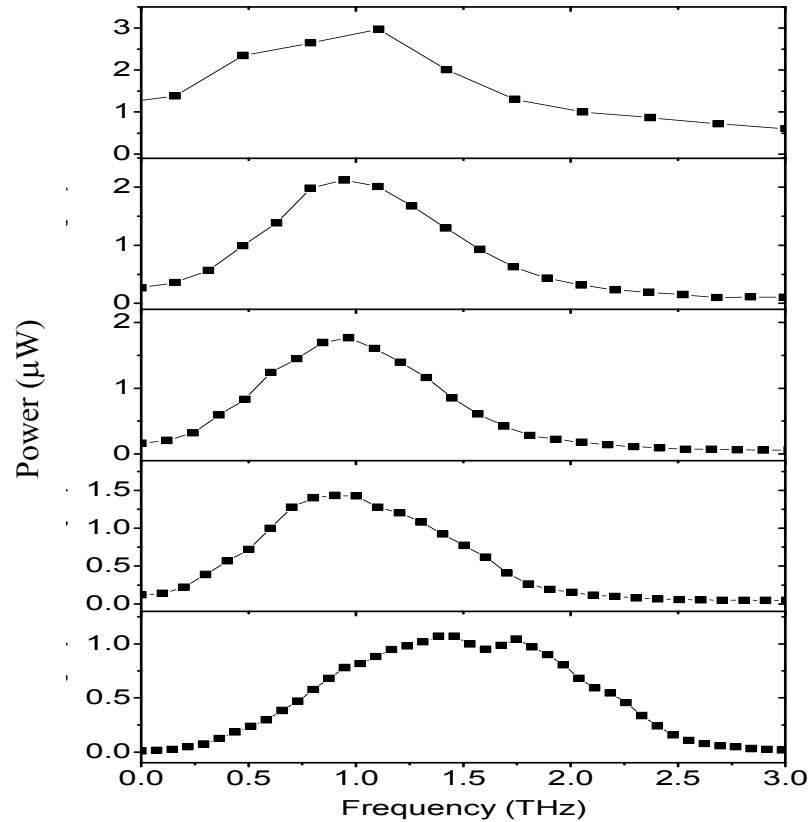


Fig 3.7: Power vs. THz frequency for Various Pulse Durations. From top to bottom, the durations are  $\tau = 1.06, 2.13, 2.78, 3.35,$  and  $4.61$  ps.

Fig 3.7 shows the emitted THz power as a function of frequency adjusted by the delay time for a variety of optical pulse durations,  $\tau = 1.06, 2.13, 2.78, 3.35,$  and  $4.61$  ps. As the pulse duration is increased, the peak power of the THz radiation is reduced:  $3 \mu\text{W}$  for  $\tau = 1.06$  ps and  $1 \mu\text{W}$  for  $\tau = 4.61$  ps. For the pulses shorter than  $3.35$  ps the maximum power is obtained near  $1$  THz and the tuning range is between  $0.5$  and  $1.5$  THz. The longest pulses ( $\tau = 4.61$  ps) produce the maximum THz power around  $1.5$  THz and the frequency is tunable from  $0.7$  to  $2.2$  THz. The data shows two dips at  $1.7$

and 2.2 THz corresponding to water absorption lines. The spectral profile of the radiation power is mainly determined by two factors. First, the radiation field is a quadratic function of frequency, which accounts for the low radiation power at lower frequencies. Second, as we tune the frequency by adjusting the time delay, the two optical pulses overlap less and less in time as the frequency increases, and so for larger frequencies the THz radiation power also falls away. For the 1.06 ps pulse duration the THz power does not vanish at either high or low frequencies, because the relatively short pulses produce additional THz radiation by optical rectification. The process involves only the pulses with polarization parallel to the  $[1 -1 0]$  axis. Optical rectification gives a broadband THz emission, and is easily distinguished from the type-II DFG emission since it has a different angular dependence as the ZnTe crystal is rotated.

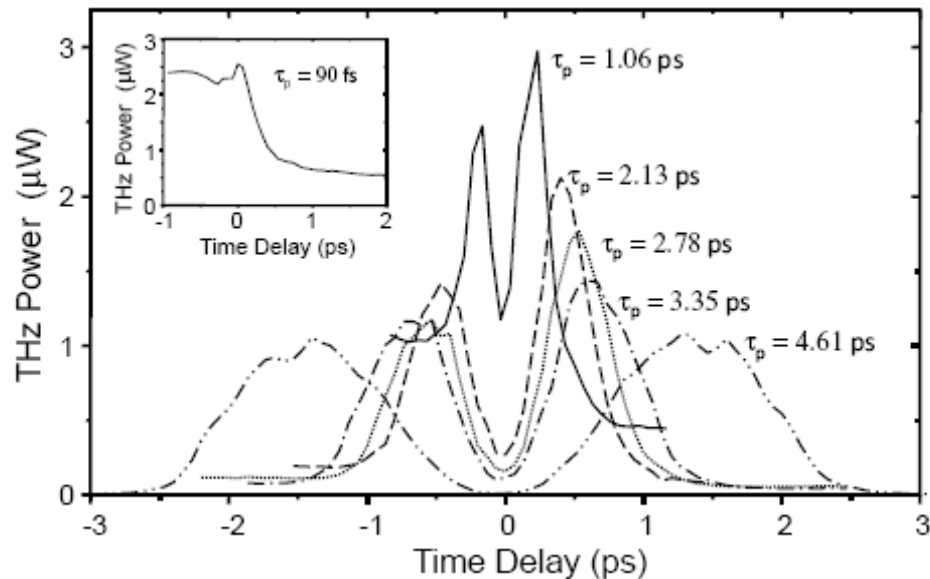


Fig 3.8: THz Power Asymmetry for Negative Delay. The inset shows the power when the pulse is unchirped and fully compressed. The THz in that run is generated through optical rectification.

Figure 3.8 shows the THz radiation power as a function of time delay. In this case, the range is extended to negative time delays, where the pulse with the polarization parallel to the  $[1 -1 0]$  axis, pulse 1, precedes the other, pulse 2. The data shows a notable imbalance of the emission for negative time delays, which can be accounted for by the anisotropy of the nonlinear absorption processes. The inset of fig. 3.8 is useful to understand this asymmetry. It shows the THz emission power for a fully compressed 90 fs pulse. In this case the whole emission is generated by optical rectification. The pulse is still sent through the splitter, so the driving pulse incident on the ZnTe crystal is two orthogonally-polarized pulses, one leading the other. In this arrangement, only the pulse 1 contributes to the THz generation by optical rectification. For positive time delays, the pulse 1 and the THz pulse are absorbed by the free carriers generated by the preceding pulse 2 through parasitic nonlinear effects, thus the THz power is lower than the one for negative time delays, where the pulse 2 has no effect. The effect diminishes as the pulse duration increases: it is still pronounced for the 1.06-ps data, visible for 2.13, 2.78, and 3.35 ps data, and negligible for 4.61 ps data. The THz power of DFG shows an opposite trend: the efficiency of THz generation is higher for positive time delays. The reason is following. Eventually, pulse 1 exerts stronger parasitic nonlinear effects than pulse 2 [19]. Therefore, the THz radiation by DFG, involving both pulses 1 and 2, sees less of the parasitic effects for a positive time than the other way around. For the longest pulse duration of 4.61ps, this asymmetry disappears.

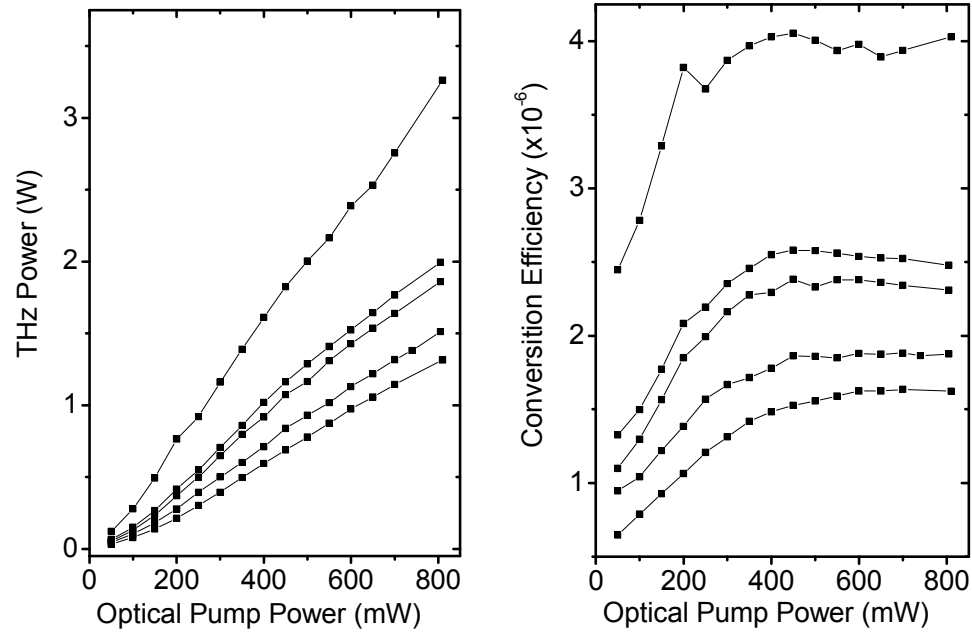


Fig 3.9 THz Power vs. Pump Power

Finally, fig. 3.9 shows the THz radiation power as a function of input optical power and the optical-to-THz conversion efficiency curves. We see that in the range of powers we used, the emitted power reached a threshold. Below this threshold with an average intensity of  $3.8 \text{ W/cm}^2$ , the THz power varies quadratically with the input power, as expected for a second-order process. Above the threshold it varies almost linearly with input power. The saturation of the conversion efficiency can be attributed to the parasitic nonlinear effects in the ZnTe crystal.

We have demonstrated an experimental scheme for generating strong, narrowband and tunable THz radiation. This arrangement is advantageous over previous incarnations for two reasons: First, no pump power is wasted in the pulse splitting device; Second, the THz generation mechanism is Type-II DFG, allowing less

parasitic nonlinear effects comparing with Type-I DFG. This tabletop source is relatively simple and compact, and can be integrated easily into an ultrafast spectroscopy setup.

## **4. THz-Driven, Nonlinear Transient Effects in Semiconductor**

### **Quantum Wells**

In recent years, the development of coherent Terahertz (THz) sources has established a new regime of semiconductor optics where internal transitions between quasi-particle states can be probed directly. Investigations have employed time-resolved spectroscopy with weak THz pulses to detect and monitor conductivity [24], the build-up of plasma screening [25] and bound exciton formation [26-30]. In parallel, it has been shown that the application of intense THz fields to semiconductors strongly modifies and controls the optical properties [31– 44].

In this context, it is interesting to study excitation of a semiconductor quantum well (QW) with an intense single-cycle THz pulse whose Rabi energy approaches the energy of the excitonic 1s-to-2p transition. Such investigations enter the regime of extreme-nonlinear optics [36, 45] where the rotating-wave approximation (RWA) breaks down. Instead, the light-induced transitions depend on both the envelope of the THz pulse and its carrier-envelope offset phase [46]. Furthermore, the contributions beyond the RWA lead to high harmonics in the spectrum. The extreme-nonlinear dynamics induced by THz excitation of a QW is particularly interesting since, in contrast to optical excitation in this regime [47], Coulomb effects remain important. Thus, new insights into the internal dynamics of excitonic QW polarization can be obtained.

## 4.1 Excitonic Structure in Semiconductor Quantum Wells

### 4.1.1 Quantum Wells in GaAs

A quantum well (QW) is a structure that traps a particle in 1 dimension. Shown in fig. 4.1, this localization gives rise to a series of discrete particle states inside the well.

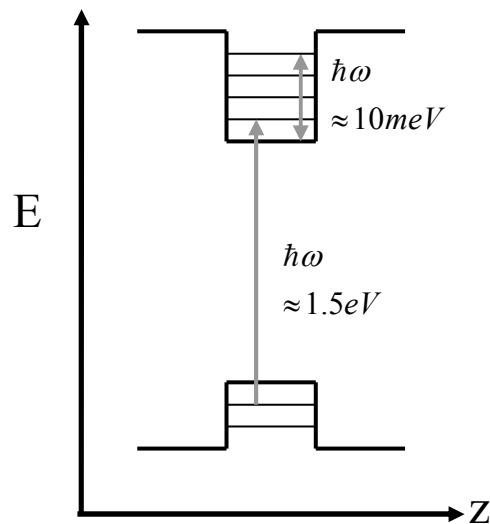


Fig 4.1: Quantum Well Potential. The hole occupies the lower band and the electron the upper. Each is trapped in the well. The excitation and intraband energies are shown.

This can be created in semiconductors by growing sheets of crystal with different composition, typically by introducing impurities into the structure. An example of this is  $\text{Al}_{0.3}\text{Ga}_{0.7}\text{As}/\text{GaAs}$  quantum wells, in which the well “boundary” regions are made of a GaAs crystal where Al is substituted for 30% of the Ga in the lattice. Such

structures confine free carriers in the GaAs sheets, which forms a quantum well in the growth direction. Typical thicknesses of the wells are on the order of tens of nanometers. The carriers are free to move in the plane of the wells, but the band structure is altered by strain and confinement so that the  $\Gamma$ -point degeneracy between light holes and heavy holes is lifted, as shown in fig. 4.2.

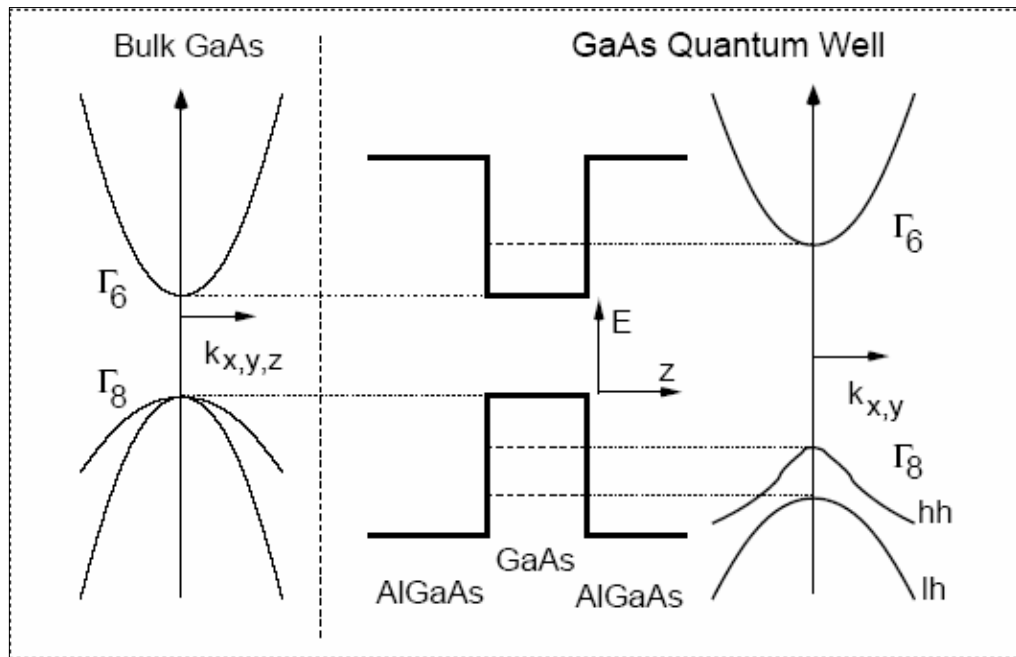


Fig 4.2: Band Structure for Carriers Traveling in the QW Plane. The left band structure is for carriers in bulk GaAs; the right is the modified structure within the quantum well.

Quantum wells are usually grown in stacks to increase their optical response. For instance, the QW sample used for THz studies in our lab was supplied by the Prineas group at the University of Iowa. It was a stack of 10 wells with GaAs thickness 11.7 nm and  $\text{Al}_{0.33}\text{Ga}_{0.67}\text{As}$  thickness 16 nm. This was grown between buffer layers of

AlGaAs on a GaAs substrate to provide protection for the nanostructure as well as mechanical strength.

Quantum wells are used in electronic studies for a number of reasons. The confinement of electrons and holes leads to strong interband transitions [48]. Additionally, the well structure gives rise to a discrete set of subbands which can be manipulated through optical means. Additionally, the confinement enhances many-body effects and carrier-carrier scattering [49].

#### 4.1.2 Excitons

When an electron is excited from the valence band it leaves a positively charged hole behind. These two particles interact through Coulomb forces, and can form a bound state called an exciton. In GaAs, the electron effective mass is  $0.067m_e$  and the hole effective mass is  $0.34m_e$ , giving a reduced mass of  $\mu = 0.0226m_e$ . With a dielectric constant of 12.9, a simple calculation gives a Bohr radius of

$$a = a_0 \epsilon \frac{m_e}{\mu} = 13 \text{ nm} \quad (4.1.1)$$

corresponding to about 23 times the GaAs lattice constant of 0.56 nm. This is sufficiently large that a first-order calculation can be made for the excitonic states which treats the lattice potential as a somewhat smooth background.

Schrödinger's equation for the electron-hole system is

$$\left[ -\frac{\hbar^2}{2\mu} \nabla^2 + V(\vec{r}) \right] \psi(\vec{r}) = E\psi(\vec{r}) \quad (4.1.2)$$

In cylindrical coordinates, this becomes

$$-\frac{\hbar^2}{2\mu} \left[ \frac{1}{r} \frac{\partial}{\partial r} \left( r \frac{\partial f}{\partial r} \right) + \frac{1}{r^2} \frac{\partial^2 f}{\partial \theta^2} + \frac{\partial^2 f}{\partial z^2} \right] \psi(\vec{r}) + (V(\vec{r}) - E) \psi(\vec{r}) = 0 \quad (4.1.3)$$

To simplify the analysis, I make the approximation that the potential is a hard-walled quantum well potential in the  $z$  direction, and that the Coulomb potential between the two particles depends only on the polar radius  $r$ , and not  $z$ . Since the well length ( $\sim 10$  nm) is much narrower than the estimated Bohr radius, this should give a reasonable approximation. In this case, it is possible to separate variables so that

$$\psi(\vec{r}) = R(r)\Phi(\phi)Z(z) \quad (4.1.4)$$

The solution in the  $z$  direction is

$$Z(z) = \sin(k_z z) \quad (4.1.5)$$

where

$$k_z = \frac{\pi n}{l} \quad \text{for } n = 1, 2, 3, \dots \quad (4.1.6)$$

and  $l$  is the thickness of the well. In the polar variable, the solution is

$$\Phi(\phi) = e^{\pm im\phi} \quad \text{for } m = 1, 2, 3, \dots \quad (4.1.7)$$

From here we can see that the states are canonical quantum well states in the  $z$  direction, and similar to hydrogen states in the polar variable, containing a well-defined angular momentum. The remaining equation for the radial part is

$$\frac{\partial^2 R}{\partial r^2} + \frac{1}{r} \frac{\partial R}{\partial r} - \left( k_z^2 - \frac{2\mu}{\hbar^2} E + \frac{m^2}{r^2} - \frac{2\mu}{\hbar^2} \frac{e^2}{4\pi\epsilon\epsilon_0 r} \right) R(r) = 0 \quad (4.1.8)$$

This is identical to the radial part of the Schrödinger equation for the hydrogen atom with the substitutions  $l(l+1) \rightarrow m^2$  and  $E \rightarrow E - \frac{p_z^2}{2\mu}$ . The radial quantum number must also be modified so that  $n \rightarrow n - 1/2$ . The result of these differences is that the energy levels go as

$$E_n = -\frac{E_R}{\left(n - \frac{1}{2}\right)^2} \quad (4.1.9)$$

instead of  $E_n = -E_R / n^2$  as in the 3D case. Additionally, the orbital radii follow the form  $a_n = a_0(n - 1/2)$ .

For this reason, the excitonic states are often called hydrogenic. They have well defined angular momentum states which can be labeled  $s, p, d, f, \dots$  in accordance with the hydrogen conventions. The values for  $m$  are constrained so that  $m < n$ , where  $n$  is the radial quantum number. Because of the lower effective mass and screening from the lattice, the binding energy of GaAs QW excitons is about 10 meV, and the  $1s - 2p$  transition energy is  $8.9 \text{ meV} \approx 2 \text{ THz}$ . It is notable that the orbital radius for the  $1s$  state is half of that of the exciton in bulk GaAs. Likewise, the binding energy is four times the 3D excitonic energy. The constraint in the  $z$ -direction enhances the electron-hole interaction.

## 4.2 Experimental Investigation

### 4.2.1 Experimental Arrangement

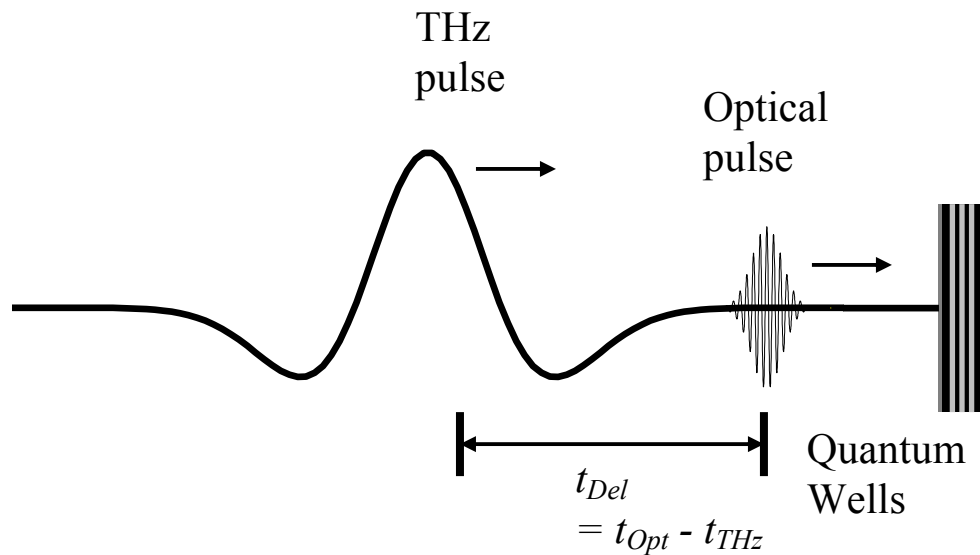


Fig 4.3: Experimental Arrangement for THz-Driven Spectral Modulation.

Here I present an experiment-theory investigation of a pump-probe measurement using a strong single-cycle THz pulse and a weak optical probe to study time-resolved nonlinear effects in the optical spectrum in multiple GaAs/AlGaAs QWs. The experiments were conducted at OSU, and the theoretical calculations made by M. Kira working in the theoretical group of S.W. Koch in Marburg, Germany. A schematic of the experimental setup is shown in fig. 4.3. The measurements were performed using 805-nm, 100-fs pulses from a 1-kHz Ti:sapphire regenerative amplifier (Coherent Inc., Legend). The optical beam was split into two components: the major portion for THz

generation and the minor portion for the optical probe. Single-cycle THz pulses were generated by optical rectification in a 1-mm ZnTe crystal. The incident optical pulse energy was 0.8 mJ, irradiated on a roughly 3-mm spot in the ZnTe crystal. The THz pulses were collimated with an off-axis parabolic mirror and the THz beam diameter was 1.5 mm at the focus. The THz pulse shape was measured using electro-optic sampling in a 1-mm ZnTe crystal. The absolute THz power was determined using a silicon bolometer at liquid helium temperature. The THz electric-field amplitude at the peak is estimated at 10 kV/cm when the optical pump pulse energy is 0.8 mJ.

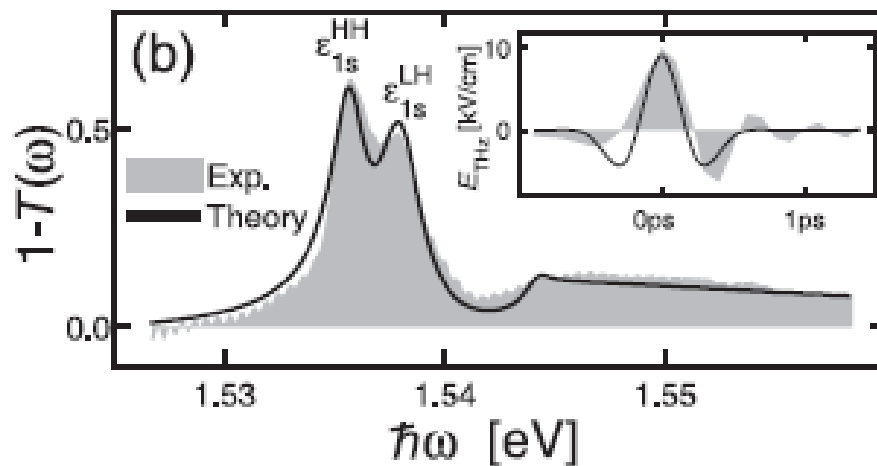


Fig. 4.4:  $1-T(\omega)$  for the QW sample. The solid line is the calculated value, the shaded area the experimental measurement.

We put a GaAs QW sample at the focus of the THz pulses and measured the optical transmission spectra. The sample studied had ten high-quality, undoped 12-nm wide GaAs wells separated by 16-nm-wide  $Al_{0.3}Ga_{0.7}As$  barriers. Fig 4.4 shows the  $1-T(\omega)$  spectrum of the sample. This is somewhat like an absorption spectrum, but the spectrally-resolved reflection was not measured, and so it is not a true absorption

spectrum. The spectrum is analyzed combining Koch's standard microscopic theory [50] with a  $\mathbf{k}\cdot\mathbf{p}$ -bandstructure calculation including the heavy-hole (HH) and light-hole (LH) valence bands as well as the strain inside the sample. The results are shown as a solid line in fig 4.4.

The sample was excited by strong THz pulses (inset to Fig. 4.4) and probed by weak optical pulses having central times  $t_{\text{THz}}$  and  $t_{\text{opt}}$ , respectively. I measured the spectrally-resolved intensity of the optical pulse as function of the delay  $\Delta t = t_{\text{THz}} - t_{\text{opt}}$  yielding the normalized transmission probability  $T(\omega, \Delta t)$ . The THz induced changes are obtained as the differential spectrum  $\Delta T \equiv T(\omega) - T(\omega, \Delta t)$ .

#### 4.2.2 Calculation of Spectral Modulation

The theoretical description of the nonlinear experiment follows from the standard many-body Hamiltonian [50] for the Coulomb-interacting carriers that are coupled to light via the minimal-substitution Hamiltonian [51-54]. To obtain the optical response under the influence of an intense THz excitation, we solve the generalized multi-band Semiconductor-Bloch Equations for the microscopic polarization  $P_{\vec{k}}^{\alpha}$  with carrier momentum  $\vec{k}$  between conduction band and valence band  $\alpha$

$$\begin{aligned}
 i\hbar \frac{\partial}{\partial t} P_{\vec{k}}^{\alpha} = & \left( \varepsilon_{\vec{k}}^{\alpha} - j_{\vec{k}}^{\alpha} A_{\text{THz}} + \frac{e^2}{2\mu^{\alpha}} A_{\text{THz}}^2 \right) P_{\vec{k}}^{\alpha} \frac{\partial^2 \Omega}{\partial u^2} \\
 & - \left( 1 - f_{\vec{k}}^e - f_{\vec{k}}^{h,\alpha} \right) \left[ d_{\vec{k}}^{\alpha} E_{\text{opt}} + \sum_{\vec{k}'} V_{\vec{k}-\vec{k}'}^{\alpha} P_{\vec{k}'}^{\alpha} \right] \\
 & + \text{scattering.}
 \end{aligned} \tag{4.2.1}$$

Here,  $\varepsilon_{\vec{k}}^a$  contains the kinetic energy of the single conduction- and multiple valence-band carriers having occupations  $f_{\vec{k}}^e$  and  $f_{\vec{k}}^{h,\alpha}$ , respectively. Furthermore,  $d_{\vec{k}}^a$  is the interband dipole-matrix element,

$$j_{\vec{k}}^{\alpha} \equiv -\frac{|e|}{\hbar} \frac{\partial \varepsilon_{\vec{k}}^{\alpha}}{\partial |\vec{k}|} \cos \phi_{\vec{k}} \quad (4.2.2)$$

is the current-matrix element with the angle  $\phi_{\vec{k}}$  between  $\vec{k}$  and polarization direction of the THz field, and  $\mu^a$  is the effective reduced mass [54, 55]. We evaluate  $\varepsilon_{\vec{k}}^a$ ,  $d_{\vec{k}}^a$ ,  $j_{\vec{k}}^{\alpha}$ ,  $\mu^a$  and the Coulomb-matrix element  $V_{\vec{k}}^{\alpha}$  using the wavefunctions from the  $\mathbf{k}\cdot\mathbf{p}$ -bandstructure calculation. The presence of carriers and the coupling to phonons and disorder lead to scattering of the polarization. Since excitation-induced dephasing [53, 56] is not appreciable for the weak optical excitation used, we implement scattering via a constant dephasing.

The polarization couples to both the optical electric field  $E_{\text{opt}}$  and the THz vector potential  $A_{\text{THz}}$  at the QW position. The term proportional to  $dE_{\text{opt}}$  describes the optical generation of polarization whereas the two terms containing  $A_{\text{THz}}$  describe intraband processes. The  $A^2$ -dependent renormalization of the kinetic energies is always positive and it can be directly related to the so called ponderomotive energy [31]. The ponderomotive energy can be understood conceptually by considering the classical case of a free electron in an oscillating electric field given by

$$E(\omega) = E_0 \cos \omega t \quad (4.2.3)$$

Using  $F = ma$ , the equation of motion for the electron is

$$\ddot{x} = -\frac{e}{m} E_0 \cos \omega t \quad (4.2.4)$$

The solution to which is

$$x(t) = \frac{eE_0}{m\omega^2} \cos \omega t \quad (4.2.5)$$

The average kinetic energy of the electron is

$$\begin{aligned} \langle KE \rangle &= \left\langle \frac{1}{2} m \dot{x}^2 \right\rangle = \frac{1}{2} \frac{e^2 E_0^2}{m\omega^2} \langle \sin^2 \omega t \rangle \\ &= \frac{e^2 E_0^2}{4m\omega^2} \end{aligned} \quad (4.2.6)$$

which is often called the ponderomotive energy. It represents the energy charged particles gain when placed in an oscillating field. Importantly, it is always positive and always increases the particle energies.

The strong THz pulse couples to the optical polarization via the  $j^\alpha A_{THz}$  term that has a different parity than the purely optically generated polarization since  $j_{-\vec{k}} = -j_{\vec{k}}$ . Thus, the experimental single-cycle THz pulse converts the initially s-like polarization into  $p$ -,  $d$ -, . . . like contributions via linear and nonlinear transitions. The transition frequencies between the different excitonic states fall into the region of a few THz, e.g.  $\nu_{2p}^{HH} - \nu_{1s}^{HH} = 1.96$  THz and  $\nu_{2p}^{LH} - \nu_{1s}^{LH} = 1.65$  THz where  $\epsilon_\lambda = h\nu_\lambda$  is the energy of state  $\lambda$ . These THz-induced transitions can be observed as large changes in the differential spectrum  $\Delta T(\omega, \Delta t)$ .

Treatment of the light propagation through the experimental multiple well structure was accomplished by solving Maxwell's wave equation via a transfer-matrix technique [57]. The theoretical vector potential

$$A_{THz}(t) = A_0 \exp\left[-\left(\frac{t}{\tau}\right)^2\right] \cos(2\pi\nu_{THz}t + \phi) \quad (4.2.7)$$

was matched to the experimental single-cycle THz pulse choosing the central frequency  $\nu_{THz} = 0.9$  THz, carrier-envelope offset phase  $\phi = \pi/2$ , duration  $\tau = 300$  fs, and  $A_0$  such that the peak strength of the electric field is 9.2 kV/cm.

At the pulse peak we note the ratios between the Rabi energy  $h\nu_R$  and the  $1s-2p$  transition energy are  $\nu_R^{HH} / \nu_{2p-1s}^{HH} = 0.63$  and  $\nu_R^{LH} / \nu_{2p-1s}^{LH} = 0.79$ . These values are clearly in the regime of extreme-nonlinear optics where one expects ultrafast nonlinearities.

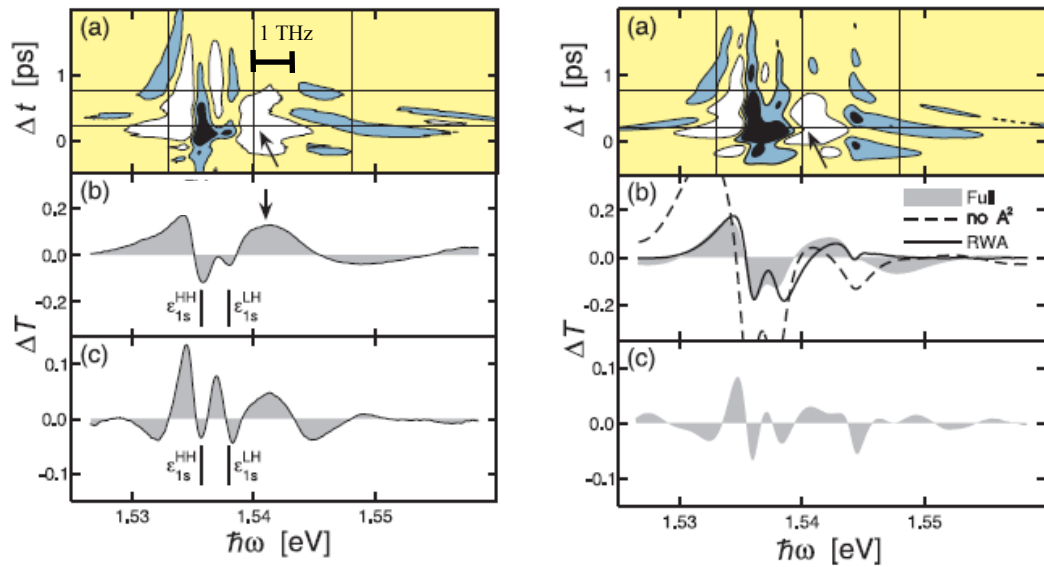


Fig 4.5: Differential Transmission Spectra. I) Measured differential transmission. II) Calculated differential transmission. In the top pane of each panel, the vertical axis is pump-probe delay, the horizontal axis is photon energy. The horizontal lines in the top panes mark cross sections at times  $\Delta t = 0.22$  ps and  $0.78$  ps, which are shown in panes b) and c).

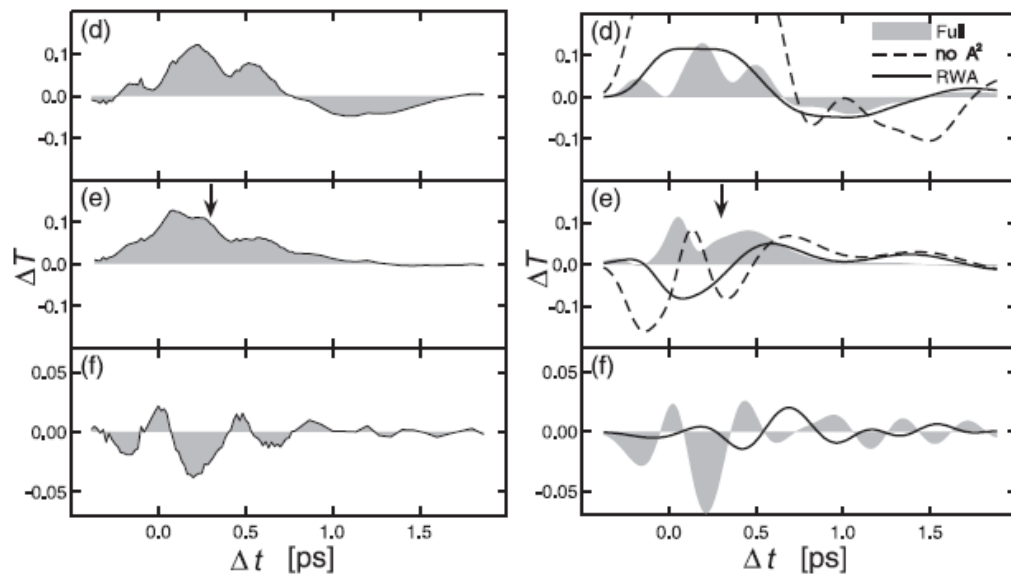


Fig 4.6: Differential Transmission vs. Time. I) Measured differential transmission. II) Calculated differential transmission. Each pane corresponds to a vertical section of 4.5-a. d, e, and f correspond to  $1.533$  eV,  $1.540$  eV, and  $1.548$  eV, respectively.

Figures 4.5 I(a) and 4.5 II(a) show the experimental and theoretical  $\Delta T$  as a function of optical energy  $\hbar\omega$  and time delay  $\Delta t$ . The horizontal lines indicate energy cross sections and the vertical lines time slices for fixed energies. A comparison of Figs. 4.5 I and 4.5 II shows that the theory excellently reproduces not only the magnitude of the essential features in  $\Delta T$ ; but also their spectral and temporal shapes.

We note that the THz-induced features are strong – changes are almost 50% of the linear  $T$  in Fig. 4.4 – and several transient  $\Delta T$  signatures appear on an ultrafast sub-picosecond time scale. As we discuss in the following paragraphs, the experimental signal contains well-defined characteristics of (i) ponderomotive contributions, (ii) signatures of the excitonic dynamical Franz- Keldysh effect [34] , and (iii) large deviations from the RWA including THz harmonic generation. Performing a detailed switch-off analysis, the theory clearly identifies the physical origin of the different  $\Delta T$  contributions.

In both Figs. 4.5 I(a) and 4.5 II(a), we observe for small time delays ( $\Delta t_b = 0.22$  ps) a positive  $\Delta T$  (white region with arrow) that exists transiently for about 500 fs – shorter than the other transients around the 1s resonances. This feature is energetically slightly above the 1s- LH resonance at  $\hbar\omega_c = 1.540$  eV. In the cross-sections (b) and (e) in Figs. 4.5 I and II this feature is indicated by an arrow. To reveal its origin, Figs. 4.5 II(b) and 4.6 II(e) compare the full computation (shaded area) with calculations where either the  $A^2$  term in eq. 4.2.1 is switched off (dashed line) or the RWA is applied (solid line). Without the  $A^2$  term the positive ultrafast  $\Delta T$  feature is nearly washed out and the overall shape of the experimental  $\Delta T$  is not reproduced at all. Thus,

we can directly link this ultrafast transient to the presence of the ponderomotive  $A^2$  contribution of the single-cycle THz pulse. As shown in eq. (4.2.6), the  $A^2$  term can be interpreted classically as the kinetic-energy change of the electron in a strong electromagnetic field. As this energy is quadratic in  $A_{\text{THz}}$ , it is clear that this feature is shorter-lived than the other transients.

In addition, we find that the non-RWA contributions are needed to obtain the correct oscillatory shape of  $\Delta T$  around the ponderomotive  $\Delta T$  transient, demonstrating the extreme nonlinearity of the induced  $\Delta T$ . In both experiment and theory, the shape of  $\Delta T$  suggests that the excitonic 1s-HH resonance in  $T$  is redshifted whereas the 1s-LH resonance in  $T$  is blueshifted for early and redshifted for later delay times due to the THz pulse. Comparing in Fig. 4.5 II(b) calculations with (shaded area) and without (dashed line) the  $A^2$  term shows that the ponderomotive term contributes as a compensating blueshift. In particular, the blueshift of the excitonic 1s-LH resonance in  $T$  for early delay times can only be explained when the  $A^2$  term is included. These observations are in agreement with earlier investigations [33–35] of the excitonic dynamical Franz-Keldysh effect for continuous-wave THz excitations. For small delay times, the THz interaction with the optical polarization is strongest and the ponderomotive  $A^2$  dominates causing an overall blueshift for the 1s-LH resonance. At later delay times, this resonance is redshifted. This can be viewed as a manifestation of the AC stark effect.

In the AC Stark effect, the excitonic 1s and 2p states couple to the electromagnetic field. As a result of this coupling, the energy eigenstates become “dressed”, lowering

the energy of the  $1s$  state and increasing the energy of the  $2p$  state. This causes an overall redshift of the  $1s$  resonance. In the Hamiltonian, the AC stark effect arises from the  $j_k^\alpha A_{THz}$  term, which is linear in the field, as opposed to the  $A^2$  term. For later delay times, the field becomes weaker, and the term linear in  $A$  dominates over the term quadratic in  $A$ , resulting in a redshift of the resonance.

Figure 4.6 II(d) displays the temporal evolution of  $\Delta T$  at the energy  $\hbar\omega_d = 1.533$  eV that is below the  $1s$ -HH resonance. Again, the full computation (shaded area) reproduces the experimentally measured [Fig. 4.6 I(d)] features. When we switch off either the  $A^2$  contribution (dashed line) or apply the RWA (solid line), the result no longer agrees with the experiment. We observe again that the  $A^2$  and the  $jA$  contributions compensate each other. In addition, the fast oscillations in  $\Delta T$  induced by non-RWA parts clearly indicate that the experiment is in the regime of extreme-nonlinear excitations as the dynamics is determined by the full oscillations of the THz pulse and not only by its envelope. The theoretical analysis confirms that the actual positions of the oscillations in  $\Delta T$  can be controlled by the carrier-envelope offset phase.

As a last feature, we investigated  $\Delta T$  at  $\hbar\omega_f = 1.548$  eV where shallow resonance features are centered at the energy matching  $\varepsilon_{1s} + \Delta / 2 + 2\hbar\nu_{THz}$ ; where  $\Delta$  is the detuning of the THz pulse with respect to the  $1s$ - $2p$  transition. Since the THz spectrum – the bar in Fig. 4.5 I(b) indicates the full width at half maximum – is much narrower than the extension of the high energy features, we can rule out the explanation that they arise due to absorption of a single THz photon. These features are best explained

by THz-frequency third harmonic generation, since one needs the absorption of two additional THz photons, a contribution which is neglected in the RWA. Figure 4.6 II(f) presents  $\Delta T(\omega_f, \Delta t)$  for the full computation (shaded area) and with the RWA (solid line). Only residual oscillations are observed with the RWA; for slightly longer THz pulses these residual oscillations vanish altogether. Since the oscillatory features are at the correct energetic position and require non-RWA contributions, these experimental features can also be connected to extreme nonlinearities. Our theoretical analysis shows that the positions of the  $\Delta t$ -dependent oscillations of  $\Delta T$  depend on the carrier envelope offset phase  $\phi$  and that the spectral position depends on the central frequency of the THz pulse [39].

In conclusion, we performed experimental and theoretical investigations of the interaction of strong single-cycle THz pulses with semiconductor QWs. The measured spectra are excellently reproduced by the results of our microscopic calculations. A detailed switch-off analysis clearly identifies extreme-nonlinear effects including ponderomotive contributions and THz harmonics.

## 5. Conclusion

In the Lee laboratory we have been examining quantum well structures as a model system to study electron dynamics. Semiconductor quantum wells, as well as excitonic states within them, show promise for a number of reasons. The states are relatively simple to calculate, making computational/experimental studies possible. They form discrete subbands, and can often be treated as two or three level systems. In high quality well systems, decoherence times are long enough to probe/manipulate the system through ultrafast spectroscopic means. In AlGaAs/GaAs wells, for instance, the coherence time is  $\sim 2\text{-}3$  ps [50], much longer than the 10 – 100 fs pulses which can be created in a tabletop apparatus. This reveals interesting possibilities for coherent control experiments.

As mentioned in earlier chapters, the typical transition energies of these systems lie in the THz regime. To exploit this, we have developed a number of methods for generating and shaping THz pulses. Many of these schemes use emission from orientation-patterned lithium niobate to emit specific kinds of THz pulses [1, 19, 20]: Examples include chirped pulses,  $0\text{-}\pi$  pulses, elliptically polarized pulses, etc. Complementing these techniques is the DFG method we developed, which has a fairly good conversion efficiency and quality, giving narrowband pulses with field strengths on the order of  $\sim 1$  kV/cm at 2 THz.

The Rabi frequencies of these pulses are comparable to the transition energies of excitonic states in quantum wells. This introduces the possibility that they can be used to coherently control the states. For instance, one could apply a series of  $\pi/2$  pulses to do photon echo studies of homogeneous coherence times; or use a  $\pi$  pulse to prepare

excitons in a  $2p$  state. We have shown through the quantum well study of chapter 4 that excitonic orbitals can be manipulated with a single-cycle THz pulse. A natural direction for further study is to use narrowband and shaped pulses as a more precise tool. This could prove fruitful for applications in quantum computing and quantum cryptography, as well as more traditional material studies such as carrier-carrier interactions and dephasing characteristics.

- [1] J. R. Danielson, N. Amer, and Yun-Shik Lee, “*Interaction of Strong Single-Cycle Terahertz Pulses with Semiconductor Quantum Wells*,” *Appl. Phys. Lett.*, **89**, 211118 (2006).
- [2] J. R. Danielson, Y.-S. Lee, J. P. Prineas, J. T. Steiner, M. Kira, and S. W. Koch, “*Interaction of Strong Single-Cycle Terahertz Pulses with Semiconductor Quantum Wells*,” *Phys. Rev. Lett.*, **99**, 237401 (2007)
- [3] P. Y. Han, G. C. Cho, and X.-C. Zhang, “*Time-domain transillumination of biological tissues with terahertz pulses*,” *Opt. Lett.* **25**, 242-244, (2000).
- [4] B. B. Hu and M. C. Nuss, “*Imaging with terahertz waves*,” *Opt. Lett.* **20**, 1716-1720, (1995).
- [5] P. H. Bolivar, M. Brucherseifer, M. Nagel, H. Kurz, A. Bosserhoff, and R. Buttner, “*Label-free probing of genes by time-domain terahertz sensing*,” *Phys. Med. Biol.* **47**, 3815-3821 (2002).
- [6] J. F. Federici, D. Gary, R. Barat, D. Zimdars, “*THz Standoff Detection and Imaging of Explosives and Weapons*,” *Proc. SPIE 5781*, **75** (2005).
- [7] C. J. Strachan , P. F. Taday , D. A. Newnham , K. C. Gordon , J. Axel Zeitler , M. Pepper , T. Rades, “*Using terahertz pulsed spectroscopy to quantify pharmaceutical polymorphism and crystallinity*,” *Journ. Pharm. Sciences* **94**, 837-846 (2005).
- [8] H. Harde, S. Keiding, and D. Grischkowsky, “*THz commensurate echoes: Periodic rephasing of molecular transitions in free-induction decay*,” *Phys. Rev. Lett.* **66**, 1834–1837 (1991).
- [9] M. van Exter, Ch. Fattinger, and D. Grischkowsky, “*Terahertz time-domain spectroscopy of water vapor*,” *Opt. Lett.* **14**, 1128 (1989)
- [10] M. Nagel, P. H. Bolivar, M. Brucherseifer, H. Kurz, A. Bosserhoff and R. Büttner, “*Integrated THz technology for label-free genetic diagnostics*,” *Appl. Phys. Lett.* **80**, 154-156 (2002).
- [11] R. W. McGowan, G. Gallot, and D. Grischkowsky, “*Propagation of ultrawideband short pulses of terahertz radiation through submillimeter-diameter circular waveguides*,” *Opt. Lett.* **24**, 1431, (1999).
- [12] Evans, K. F., Evans, A. H., Nolt, I. G., Marshall, B. T., “*The Prospect for Remote Sensing of Cirrus Clouds with a Submillimeter-Wave Spectrometer*,” *Journal of Applied Meteorology*, **38**: 514-525 (1999).

- [13] W.G. Mankin, J.A. Eddy, R.M. MacQueen, R.H. Lee, and C.W. Querfeld, “*Observations of Far Infrared Atmospheric Windows at  $44\text{ cm}^{-1}$  and  $50\text{ cm}^{-1}$  from Pikes Peak*”, *Nature Physical Science*, **245**, pp. 8-9, 1973.
- [14] C.H. Townes and G. Melnick, “*Atmospheric Transmission in the FarInfrared at the South Pole and Astronomical Applications*”, *PASP*, **102**, pp. 357-367, 1989.
- [15] M. Nagaia, K. Tanaka, H. Ohtake, T. Bessho, T. Sugiura, T. Hirosumi, and M. Yoshida, “*Generation and detection of terahertz radiation by electro-optical process in GaAs using  $1.56\text{ }\mu\text{m}$  fiber laser pulses*,” *Appl. Phys. Lett.* **85**, 3974 (2004).
- [16] G. Gallot, J. Zhang, R. W. McGowan, T.-I. Jeon, and D. Grischkowsky, “*Measurements of the thz absorption and dispersion of ZnTe and their relevance to the electro-optic detection of THz radiation*,” *Appl. Phys. Lett.*, vol. 74, pp. 3450–3451, June 1999.
- [17] Boyd, Robert W., *Nonlinear Optics*, 2nd Ed., Academic Press, New York, 2003
- [18] W. Hurlbut, Yun-Shik Lee, K. L. Vodopyanov, P. S. Kuo, and M. M. Fejer, “*Multi-photon absorption and nonlinear refraction of GaAs in the mid-infrared*,” *Opt. Lett.* **32**, 668 (2007).
- [19] S. Casalbuoni, H. Schlarb, B. Schmidt, P. Schmüser, B. Steffen, A. Winter, “*Numerical Studies on the Electro-Optic Sampling of Relativistic Electron Bunches*,” TESLA Report 2005-1
- [20] N. Amer, W. C. Hurlbut, B. J. Norton, Yun-Shik Lee, S. L. Etringer, and B. K. Paul, “*Terahertz wave propagation in one-dimensional periodic dielectrics*,” *Appl. Opt.* **45**, 1857-1860 (2006).
- [21] F. Zernike and P.R. Berman, “*Generation of far infrared as a difference frequency*,” *Phys. Rev. Lett.* **15**, 999 - 1001 (1965)
- [22] E. R. Brown, K. A. Smith and K. A. McIntosh, “*Coherent Millimeter-wave Generation by Heterodyne Conversion in Low-temperature-grown GaAs Photoconductors*,” *J. Appl. Phys.* **73** (1993) 1480
- [23] A. S. Weling and D. H. Auston, “*Novel sources and detectors for coherent tunable narrow-band terahertz radiation in free space*,” *J. Opt. Soc. Am. B* **13**, 2783 (1996).
- [24] R. Groeneveld and D. Grischkowsky, “*Picosecond time-resolved far-infrared experiments on carriers and excitons in GaAs-AlGaAs multiple quantum wells*,” *J. Opt. Soc. Am. B* **11**, 2502 (1994).

- [25] R. Huber, F. Tauser, A. Brodschelm, M. Bichler, G. Abstreiter and A. Leitenstorfer, “*How many-particle interactions develop after ultrafast excitation of an electron–hole plasma,*” *Nature (London)* **414**, 286 (2001).
- [26] R. A. Kaindl, M. A. Carnahan, D. Hägele, R. Lövenich and D. S. Chemla, “*Ultrafast terahertz probes of transient conducting and insulating phases in an electron–hole gas,*” *Nature (London)* **423**, 734 (2003).
- [27] I. Galbraith, R. Chari, S. Pellegrini, P. J. Phillips, C. J. Dent, A. F. G. van der Meer, D. G. Clarke, A. K. Kar, G. S. Buller, C. R. Pidgeon, B. N. Murdin, J. Allam, and G. Strasser, “*Excitonic signatures in the photoluminescence and terahertz absorption of a GaAs/Al<sub>x</sub>Ga<sub>1-x</sub>As multiple quantum well,*” *Phys. Rev. B* **71**, 073302 (2005).
- [28] M. Kira, W. Hoyer, T. Stroucken, and S. W. Koch, “*Exciton Formation in Semiconductors and the Influence of a Photonic Environment,*” *Phys. Rev. Lett.* **87**, 176401 (2001).
- [29] M. Kira, W. Hoyer, and S. W. Koch, “*Terahertz signatures of the exciton formation dynamics in non-resonantly excited semiconductors,*” *Solid State Commun.* **129**, 733 (2004).
- [30] S. W. Koch, M. Kira, G. Khitrova and H. M. Gibbs, “*Semiconductor excitons in new light,*” *Nature Mater.* **5**, 523 (2006).
- [31] A. P. Jauho and K. Johnsen, “*Dynamical Franz-Keldysh Effect,*” *Phys. Rev. Lett.* **76**, 4576 (1996).
- [32] G. J. Morales, Y. C. Lee, and R. B. White, “*Nonlinear Schrödinger-Equation Model of the Oscillating Two-Stream Instability,*” *Phys. Rev. Lett.* **81**, 457 (1998).
- [33] S. Hughes and D. S. Citrin, “*Creation of highly anisotropic wave packets in quantum wells: Dynamical Franz-Keldysh effect in the optical and terahertz regimes,*” *Phys. Rev. B* **59**, R5288 (1999).
- [34] A. H. Chin, J. M. Bakker, and J. Kono, “*Ultrafast Electroabsorption at the Transition between Classical and Quantum Response,*” *Phys. Rev. Lett.* **85**, 3293 (2000).
- [35] B. E. Cole, J. B. Williams, B. T. King, M. S. Sherwin and C. R. Stanley. “*Coherent manipulation of semiconductor quantum bits with terahertz radiation,*” *Nature (London)* **410**, 60 (2001).
- [36] A. H. Chin, O. G. Calderón, and J. Kono, “*Extreme Midinfrared Nonlinear Optics in Semiconductors,*” *Phys. Rev. Lett.* **86**, 3292 (2001).

- [37] C. J. Dent, B. N. Murdin, and I. Galbraith, “*Phase and intensity dependence of the dynamical Franz-Keldysh effect*,” Phys. Rev. B **67**, 165312 (2003).
- [38] A. Srivastava, R. Srivastava, J. Wang, and J. Kono “*Laser-Induced Above-Band-Gap Transparency in GaAs*,” Phys. Rev. Lett. **93**, 157401 (2004).
- [39] A. V. Maslov and D. S. Citrin, “*Optical absorption and sideband generation in quantum wells driven by a terahertz electric field*,” Phys. Rev. B **62**, 16686 (2000).
- [40] T. Müller, W. Parz, G. Strasser, K. Unterrainer, “*Pulse-induced quantum interference of intersubband transitions in coupled quantum wells*,” Appl. Phys. Lett. **84**, 64 (2004).
- [41] C. W. Luo, K. Reimann, M. Woerner, T. Elsaesser, R. Hey, and K. H. Ploog, “*Phase-Resolved Nonlinear Response of a Two-Dimensional Electron Gas under Femtosecond Intersubband Excitation*,” Phys. Rev. Lett. **92**, 047402 (2004).
- [42] S. G. Carter, V. Birkedal, C. S. Wang, L. A. Coldren, A. V. Maslov, D. S. Citrin, and M. S. Sherwin, “*Quantum Coherence in an Optical Modulator*,” Science **310**, 651 (2005).
- [43] J. F. Dynes, M. D. Frogley, M. Beck, J. Faist, and C. C. Phillips “*ac Stark Splitting and Quantum Interference with Intersubband Transitions in Quantum Wells*,” Phys. Rev. Lett. **94**, 157403 (2005).
- [44] D. Stehr, S. Winnerl, M. Helm, T. Dekorsy, T. Roch, and G. Strasser, “*Pump-probe spectroscopy of interminiband relaxation and electron cooling in doped superlattices*,” Appl. Phys. Lett. **88**, 151108 (2006).
- [45] O. D. Mücke, T. Tritschler, M. Wegener, U. Morgner and F. X. Kärtner, “*Role of the Carrier-Envelope Offset Phase of Few-Cycle Pulses in Nonperturbative Resonant Nonlinear Optics*,” Phys. Rev. Lett. **89**, 127401 (2002).
- [46] M. Wegener, Extreme Nonlinear Optics (Springer, 2006).
- [47] D. Golde, T. Meier, and S. W. Koch, “*Microscopic analysis of extreme nonlinear optics in semiconductor nanostructures*,” J. Opt. Soc. Am. B **23**, 2559 (2006).
- [48] A. Shik, Quantum Wells: Physics and Electronics of Two-Dimensional Systems, World Scientific Publishing, London, 1998.
- [49] L. Schultheis, A. Honold, J. Kuhl, K. Köhler, and C. W. Tu, “*Optical dephasing of homogeneously broadened two-dimensional exciton transitions in GaAs quantum wells*,” Phys. Rev. B **34**, 9027 (1986)

- [50] H. Haug and S. W. Koch, Quantum Theory of the Optical and Electronic Properties of Semiconductors (World Scientific Publ., Singapore, 2004 (fourth edition)).
- [51] C. Cohen-Tannoudji, J. Dupont-Roc, and G. Grynberg, Photons and Atoms - Introduction to Quantum Electrodynamics, (Wiley, 1989 (third edition)).
- [52] M. Kira, F. Jahnke, W. Hoyer and S. W. Koch, “*Quantum theory of spontaneous emission and coherent effects in semiconductor microstructures*,” Prog. Quantum Electron. **23**, 189 (1999).
- [53] M. Kira and S. W. Koch, “*Many-body correlations and excitonic effects in semiconductor spectroscopy*,” Prog. Quantum Electron. **30**, 155 (2006).
- [54] M. Kira, W. Hoyer, and S.W. Koch, “*Microscopic theory of the semiconductor terahertz response*,” phys. stat. sol. (b) **238**, 443 (2003).
- [55] J. M. Luttinger, and W. Kohn, “*Motion of Electrons and Holes in Perturbed Periodic Fields*,” Phys. Rev. **97**, 869 (1955).
- [56] F. Jahnke, M. Kira, S. W. Koch, G. Khitrova, E. K. Lindmark, T. R. Nelson, Jr., D. V. Wick, J. D. Berger, O. Lyngnes, H. M. Gibbs, and K. Tai, “*Excitonic Nonlinearities of Semiconductor Microcavities in the Nonperturbative Regime*,” Phys. Rev. Lett. **77**, 5257 (1996).
- [57] F. Jahnke, M. Ruopp, M. Kira, and S. W. Koch, “*Ultrashort pulse propagation and excitonic nonlinearities in semiconductor microcavities*,” Adv. Solid State Phys. **37**, 191 (1997).

# Appendix

## Bolometer Calibration

Our bolometer for these experiments was loaned by Konstantin Vodopyanov at Stanford University. Before it was lent to us, it had been calibrated to a black-body standard and assigned the responsivity  $9.26 \times 10^5$  V/W. In that calibration, the THz source was modulated with a 100 Hz optical chopper so that the beam was on for 5 ms, then off for 5 ms. The signal had the waveform shown in fig. A.1:

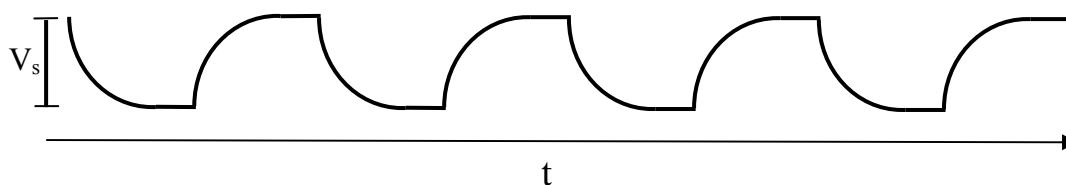


Fig A.1 CW THz signal.  $V_s$  is the measured signal.

The pulsed signal was significantly different. Rather than a CW source, the THz we measured had a repetition rate of 500 Hz or 1 KHz and a pulse duration of  $\sim 2$  -10 ps. This is much faster than the bolometer's response time, so the signal appears as a series of decaying spikes, as shown in fig. A.2:

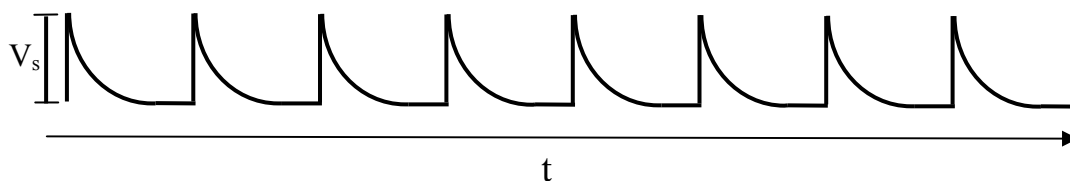


Fig A.2 Pulsed THz Signal.

This calls the bolometer's calibration into question; this is clear because the listed responsivity has units Volts/Power, but the power is poorly defined for a series of ultrashort pulses. To resolve this, I examine the time response of the bolometer to an incident beam.

The bolometer's detection crystal is a helium-cooled silicon wafer. The conductivity of the wafer is proportional to its temperature, which is itself proportional to the amount of energy deposited by the beam. The conductivity is measured and amplified by internal electronics. Specifically,

$$S = \alpha U \quad (\text{A.1})$$

where  $S$  is the signal and  $U$  the thermal energy of the crystal. With an input power  $P(t)$ , the rate equation for the system is

$$\dot{S} = \alpha \dot{U} = \alpha \left( P(t) - \frac{\beta}{\alpha} \cdot S \right) \quad (\text{A.2})$$

where  $\beta$  is the temperature decay rate. When measuring a CW source, the signal comes to equilibrium with the beam on, so that

$$\dot{S}_{CW} = 0 = \alpha \left( P - \frac{\beta}{\alpha} \cdot S_{CW} \right) \quad (\text{A.3})$$

$$\Rightarrow S_{CW} = \frac{\alpha}{\beta} P \quad (\text{A.4})$$

The difference in the signal when the beam is blocked and unblocked is measured. Importantly, it is inversely proportional to the decay rate, and the units for  $S_{CW}$  is kV/W

In the case of a pulsed source, the system is not allowed to come to equilibrium. Instead, the energy is deposited very rapidly, and the signal decays over time. The

power is appropriately represented as a delta function  $P(t) = E_0\delta(t)$  where  $E_0$  is the pulse energy. In this case, the rate equation becomes

$$\dot{S}_{pulsed} = \alpha \left( E_0\delta(t) - \frac{\beta}{\alpha} \cdot S_{pulsed} \right) \quad (\text{A.5})$$

Integrating across  $t = 0$ , the discontinuity in the signal is given by

$$\Delta S_{pulsed} = \lim_{\varepsilon \rightarrow 0} \int_{-\varepsilon}^{\varepsilon} \alpha \left( E_0\delta(t) - \frac{\beta}{\alpha} \cdot S \right) dt \quad (\text{A.6})$$

$$\Delta S_{pulsed} = \alpha E_0 \quad (\text{A.7})$$

after which it decays with the rate  $\beta$ ,

$$S(t)_{pulsed} = \alpha E_0 e^{-\beta t} \quad (\text{A.8})$$

The height of the discontinuity is what is measured for a pulsed source. This does not depend on the decay rate. In essence the energy is deposited far more rapidly than it can dissipate, so that the decay doesn't affect the initial signal. The units for  $\Delta S_{pulsed}$  is V/J, and should be greater than the CW responsivity by a factor of  $\beta$ . With a decay time of about 0.1 ms, the pulsed responsivity is  $9.26 \times 10^9$  V/J